The Superluminous Transient ASASSN-15lh as a Tidal Disruption Event from a Kerr Black Hole

G. Leloudas[1,2], M. Fraser[3], N. C. Stone[4], S. van Velzen[5], P. G. Jonker[6,7], I. Arcavi[8,9], C. Fremling[10],

J. R. Maund[11], S. J. Smartt[12], T. Krühler[13], J. C. A. Miller-Jones[14], P. M. Vreeswijk[1], A. Gal-Yam[1],

P. A. Mazzali[15,16], A. De Cia[17], D. A. Howell[8,18], C. Inserra[12], F. Patat[17], A. de Ugarte Postigo[19,2],

O. Yaron[1], C. Ashall[15], I. Bar[1], H. Campbell[3,20], T.-W. Chen[13], M. Childress[21], N. Elias-Rosa[22],

J. Harmanen[23], G. Hosseinzadeh[8,18], J. Johansson[1], T. Kangas[23], E. Kankare[12], S. Kim[24], H.

Kuncarayakti[25,26], J. Lyman[27], M. R. Magee[12], K. Maguire[12], D. Malesani[2], S. Mattila[23,28,3], C. V.

McCully[8,18], M. Nicholl[29], S. Prentice[15], C. Romero-Cañizales[24,25], S. Schulze[24,25], K. W. Smith[12],

J. Sollerman[10], M. Sullivan[21], B. E. Tucker[30,31], S. Valenti[32], J. C. Wheeler[33], D. R. Young[12]

[1]*Department of Particle Physics and Astrophysics, Weizmann Institute of Science, Rehovot 7610001, Israel*

[2]*Dark Cosmology Centre, Niels Bohr Institute, University of Copenhagen, Juliane Maries vej 30, 2100 Copenhagen, Denmark*

[3]*Institute of Astronomy, University of Cambridge, Madingley Road, Cambridge CB3 0HA, UK*

[4]*Columbia Astrophysics Laboratory, Columbia University, New York, NY, 10027, USA*

[5]*Department of Physics and Astronomy, The Johns Hopkins University, Baltimore, MD, 21218, USA*

[6]*SRON, Netherlands Institute for Space Research, Sorbonnelaan 2, 3584 CA, Utrecht, The Netherlands*

[7]*Department of Astrophysics/IMAPP, Radboud University Nijmegen, P.O. Box 9010, 6500 GL*

1

Nijmegen, The Netherlands

[8]*Las Cumbres Observatory Global Telescope Network, 6740 Cortona Dr., Suite 102 Goleta, CA 93117, USA*

[9]*Kavli Institute for Theoretical Physics, University of California, Santa Barbara, CA 93106, USA*

[10]*Department of Astronomy, The Oskar Klein Center, Stockholm University, AlbaNova, 10691, Stockholm, Sweden*

[11]*Department of Physics and Astronomy, The University of Sheffield, Hicks Building, Hounsfield Road, Sheffield, S3 7RH, UK*

[12]*Astrophysics Research Centre, School of Mathematics and Physics, Queen's University Belfast, Belfast BT7 1NN, UK*

[13]*Max-Planck-Institut für extraterrestrische Physik, Giessenbachstraße, 85748 Garching, Germany*

[14]*International Centre for Radio Astronomy Research, Curtin University, GPO Box U1987, Perth, WA 6845, Australia*

[15]*Astrophysics Research Institute, Liverpool John Moores University, IC2, Liverpool Science Park, 146 Brownlow Hill, Liverpool L3 5RF, UK*

[16]*Max-Planck Institut für Astrophysik, Karl-Schwarzschild-Str. 1, 85748 Garching b. München, Germany*

[17]*European Southern Observatory, Karl-Schwarzschild-Strasse 2, 85748 Garching, Germany*

[18]*Department of Physics, University of California Santa Barbara, Santa Barbara, CA 93117, USA*

[19]*Instituto de Astrofísica de Andalucía (IAA-CSIC), Glorieta de la Astronomía s/n, E-18008, Granada, Spain*

[20] *Department of Physics, University of Surrey, Guildford, GU2 7XH, Surrey, UK*

[21] *Department of Physics & Astronomy, University of Southampton, Southampton, Hampshire, SO17 1BJ, UK*

[22] *INAF - Osservatorio Astronomico di Padova, Vicolo dellOsservatorio 5, 35122 Padova, Italy*

[23] *Tuorla Observatory, Department of Physics and Astronomy, University of Turku, Väisäläntie 20, FI-21500 Piikkiö, Finland*

[24] *Instituto de Astrofísica, Facultad de Física, Pontificia Universidad Católica de Chile, Vicuña Mackenna 4860, 7820436 Macul, Santiago, Chile*

[25] *Millennium Institute of Astrophysics, Santiago, Chile*

[26] *Departamento de Astronomía, Universidad de Chile, Casilla 36-D, Santiago, Chile*

[27] *Department of Physics, University of Warwick, Coventry CV4 7AL, UK*

[28] *Finnish Centre for Astronomy with ESO (FINCA), University of Turku, Väisäläntie 20, FI-21500 Piikkiö, Finland*

[29] *Harvard-Smithsonian Center for Astrophysics, 60 Garden Street, Cambridge, Massachusetts 02138, USA*

[30] *The Research School of Astronomy and Astrophysics, Mount Stromlo Observatory, Australian National University, Canberra, ACT 2611, Australia.*

[31] *ARC Centre of Excellence for All-sky Astrophysics (CAASTRO), Australia*

[32] *Department of Physics, University of California, Davis, CA 95616, USA*

[33] *Department of Astronomy, University of Texas at Austin, Austin, TX 78712, USA*

When a star passes within the tidal radius of a supermassive black hole, it will be torn apart[1]. For a star with the mass of the Sun ($M_\odot$) and a non-spinning black hole with a mass $< 10^8 M_\odot$, the tidal radius lies outside the black hole event horizon[2] and the disruption results in a luminous flare[3, 4, 5, 6]. Here we report observations over a period of 10 months of a transient, hitherto interpreted[7] as a superluminous supernova[8]. Our data show that the transient rebrightened substantially in the ultraviolet and that the spectrum went through three different spectroscopic phases without ever becoming nebular. Our observations are more consistent with a tidal disruption event than a superluminous supernova because of the temperature evolution[6], the presence of highly ionised CNO gas in the line of sight[9] and our improved localisation of the transient in the nucleus of a passive galaxy, where the presence of massive stars is highly unlikely[10, 11]. While the supermassive black hole has a mass $> 10^8 M_\odot$ [12, 13], a star with the same mass as the Sun could be disrupted outside the event horizon if the black hole were spinning rapidly[14]. The rapid spin and high black hole mass can explain the high luminosity of this event.

ASASSN-15lh was discovered by the All-Sky Automated Survey for SuperNovae (ASAS-SN) on 14 June 2015 at a redshift of $z = 0.2326$. Its light curve peaked at $V \sim 17$ mag implying an absolute magnitude of $M = -23.5$ mag, more than twice as luminous as any known supernova (SN)[7]. Our long-term spectroscopic follow-up reveals that ASASSN-15lh went through three different spectroscopic phases (Figure 1). During the first phase[7], the spectra were dominated by two broad absorption features. While these features appear similar to those observed in superluminous supernovae (SLSNe; Supplementary Figure 1), their physical origin is different. The features in

SLSNe are due to O II[8, 15], but this would produce an additional strong feature at ~4,400 Å (Supplementary Figure 2) . The feature at ~4,100 Å cannot be easily identified in the tidal disruption event (TDE) framework either. Two possibilities are that it could be due to absorption of Mg II or high-velocity He II[16]. After the initial broad absorption features disappeared, the spectra of ASASSN-15lh were dominated by two emission features. A possible identification for these features is He II $\lambda\lambda 3,202$ and $4,686$ Å, which are both consistently blueshifted by ~15,000 km s^{-1} (Supplementary Figure 3). He II emission is commonly seen in optically discovered TDEs[4, 5] at different blueshifts, albeit typically at lower velocities, but it has not been seen in H-poor SLSNe. These features disappeared after day +75 (measured in rest frame from peak) and the later spectra were mostly featureless, with the exception of two emission features at ~4,000 and 5,200 Å. The spectra remained much bluer than those of SLSNe[17] for many months after the peak and never revealed nebular features, even up to day +256.

A UV spectrum obtained with the *HST* on day +168 does not show any broad features[18]. At the redshift of the host, we identified weak Ly-α absorption and disproportionally strong high-ionisation lines (N V, O VI, C IV). Combined with the weakness (or absence) of common[19] low-ionisation absorption lines (Fe II, Si II, Mg II), this aspect seems to be similar to the spectrum of ASASN-14li, the only available UV spectrum of a TDE[9] (see Methods and Supplementary Figure 4). The highly-ionised gas appears at slightly different velocities, suggesting that it could be due to material in the vicinity of the TDE and ionised by its radiation. In contrast to the case of ASASSN-14li[9], we do not observe any broad features in the UV range, but the optical spectrum is also mostly featureless at these phases.

In addition, we detect the presence of hydrogen in ASASSN-15lh. A weak Hα emission line is unambiguously detected in our highest signal-to-noise spectra (Figure 1) and in more spectra at lower significance (Supplementary Figure 3). Its presence cannot be excluded in any spectrum and its strength (equivalent width $\sim$4–8 Å) is invariable, within the present errors. The velocity of the Hα line (full-width at half-maximum (FWHM) $\sim 2,500$ km s^{-1}) is different than those of other features, implying that it is formed in a different emitting region.

The light curve evolution of ASASSN-15lh is shown in Figure 2. After the initial peak and decline, around 10 September (day $+60$), the UV started rebrightening, an effect that was more prominent in the far-UV bands[20, 21, 18]. The dense photometric follow-up with the Swift Gamma-Ray Burst Mission (*Swift*) and the Las Cumbres Observatory Global Telescope Network (LCOGT) revealed that ASASSN-15lh reached a secondary UV maximum at around $+110$ days, followed by another decline. Interestingly, after day $+100$, the colours of ASASSN-15lh remained almost constant for over 120 rest-frame days (Supplementary Figure 5). By fitting a black body to the multi-wavelength photometry of ASASSN-15lh, we are able to estimate the temperature evolution, black-body radius and bolometric luminosity (Figure 3). While the UV rebrightens and the spectrum changes, the blackbody radius decreases and the temperature increases again, stabilising at $\sim 16,000$ K. This is neither expected from a SN photosphere, nor observed for SLSNe[22, 23, 24]. However, the TDE candidate ASASSN-14ae[6] showed a very similar temperature evolution to ASASSN-15lh. Even if this happened at shorter timescales, the qualitative similarity between the evolution of the two events suggests that they might be due to the same mechanism. On the other hand, the radius of ASASSN-15lh is larger by a factor of about seven, and ASASSN-

14ae has a much stronger Hα line (Supplementary Figure 1).

By integrating the bolometric luminosity, we estimate that ASASSN-15lh had radiated a total of $1.88 \pm 0.19 \times 10^{52}$ erg (depending on the assumed bolometric correction) up to 25 May 2016 (day +288). Including kinetic energy, which can reach an additional 10^{52} erg for SLSNe[15, 25], the total energy budget approaches the theoretical limit of that which SN explosions models can accommodate[26, 27]. It is possible that UV rebrightening could occur in a SLSN, due to either strong circumstellar interaction or the ionization breakout powered by a central magnetar. However, the observed Hα line is much weaker than those in SLSNe that have shown signs of late interaction[28] (Supplementary Figure 1), and there are no features indicative of interaction in the UV spectrum. In addition, predictions for ionisation breakout suggest that the spectrum should turn nebular[26], although this might apply better to an X-ray rather than a UV breakout. Nevertheless, no detailed model has yet been calculated that can naturally explain the entire spectroscopic and photometric properties observed, either in the SN or in the TDE scenario. A single epoch of imaging polarimetry with *HST* shows low levels of polarisation[18], similar to that obtained for a SLSN[29], and suggesting an only mildly asymmetric geometry (in projection). Polarisation measurements and predictions for optical TDEs are still lacking.

Strong evidence for ASASSN-15lh being a TDE comes from its environment. H-poor SLSNe are found in blue, metal-poor dwarf galaxies with average masses of $\log_{10} M_{\star} = 8.24 \pm 0.58$ $M_{\odot}$, and none have yet been found to exceed 9.60 at $z < 1$ [10, 11]. These galaxies typically have strong emission lines, pointing to active ongoing star formation and young progenitor ages that

do not exceed a few Myr^{11}. In contrast, the host of ASASSN-15lh is a massive and passive red galaxy. By fitting the available photometry (see Methods), we estimate that the mass of the host is $\log_{10} M_\star = 10.95^{+0.15}_{-0.11} M_\odot$, with a dominant stellar population of age $3.9^{+3.2}_{-1.3}$ Gyr. The spectral energy distribution (SED) fit provides a star formation rate (SFR) of $0.05^{+0.15}_{-0.05} M_\odot$ yr^{-1}, consistent with the improved limit on SFR of $< 0.02 M_\odot$ yr^{-1} that we obtained from our highest signal-to-noise spectrum. The derived specific star formation rate of $\log sSFR < -12.5$ yr^{-1} is thus three orders of magnitude lower than in any H-poor SLSN host (Supplementary Figure 7). Furthermore, the transient is positionally coincident with the nucleus of its host. By aligning postdiscovery *HST* Advanced Camera for Surveys (ACS) images with a prediscovery image taken with the Cerro Tololo Inter-American Observatory 4 m Dark Energy Camera (Supplementary Figure 8), we were able to improve the positional accuracy[7] of ASASSN-15lh by a factor of about four, corresponding to a projected nuclear offset of 131 ± 192 pc.

It has been argued that the large host galaxy mass may imply the presence of a supermassive black hole (SMBH) that is too large to disrupt stars outside its event horizon[7]. Since the tidal radius scales as $R_{\rm t} \propto M_\bullet^{1/3}$ while the gravitational radius scales as $R_{\rm g} \propto M_\bullet$, stars can only be disrupted outside the horizon of a SMBH if the black hole is below a certain size, the Hills mass[2] $M_{\rm H}$. Larger SMBHs swallow stars whole. For a non-spinning Schwarzschild SMBH, the Hills mass is $M_{\rm H} \approx 9 \times 10^7 M_\odot r_\star^{3/2} m_\star^{-1/2}$, where $m_\star \equiv M_\star/M_\odot$ and $r_\star \equiv R_\star/R_\odot$ (see Methods). Using an empirical relationship between SMBH mass and total stellar mass for elliptical and spiral/lenticular galaxies with classical bulges[12], we find $\log_{10} M_\bullet = 8.88 \pm 0.60 M_\odot$, far above the Schwarzschild Hills mass for solar-mass stars. Using an $M_\bullet - L$ relation for early-type galaxies[13],

we obtain $\log_{10} M_\bullet = 8.50 \pm 0.52\ M_\odot$. However, M_H increases by almost an order of magnitude

for rapidly spinning Kerr SMBHs and favorable orbital orientations[14]. For an optimal (prograde

equatorial) orbit and our range of SMBH mass estimates, we find that a solar-mass star can be

disrupted by a SMBH with dimensionless spin parameter $a_\bullet = 0.68$ if $\log_{10} M_\bullet = 8.28\ M_\odot$, and

by a SMBH with dimensionless spin parameter $a_\bullet = 1$ if $\log_{10} M_\bullet = 8.86\ M_\odot$. We show the

exact relativistic $M_H(a_\bullet)$ in Figure 4. For stars less massive than the Sun, the spin is constrained

to even higher values. ASASSN-15lh could be compatible with a TDE by a Schwarzschild SMBH

provided $M_\star \gtrsim 3 M_\odot$. However, the typical tidally-disrupted star comes from the lower end of

the stellar mass function, and this hypothesis is further challenged by the old age of the galaxy's

stellar population[30, 31]. Observations of active galactic nuclei suggest that rapid SMBH spins are

common[32]. We demonstrated here that TDEs present a method to probe the SMBH spins of qui-

escent galaxies. Given the inferred rapid spin of the SMBH, the fact that we did not detect a jet at

radio wavelengths implies that black hole spin alone is not sufficient to launch powerful jets (see

Methods).

The luminosity and energetics of ASASSN-15lh are also explained by a particularly massive

SMBH. The expected radiative efficiency of accretion increases from $\eta \approx 0.05$ (for a Schwarzschild

SMBH) to $\eta \approx 0.42$ for a rapidly spinning SMBH disrupting stars on prograde, near-equatorial

orbits. A particularly massive SMBH is further biased towards disrupting the most massive stars

near the main sequence turn-off mass, increasing accretion rates and total energy release. Finally,

it is known that most TDEs only release a small fraction of $\eta M_\star c^2$ in accretion power (the so-

called "missing energy problem" [30, 33]). One compelling explanation for this is that circularization

of debris and formation of the accretion disk is mediated by relativistic apsidal precession, and that the majority of TDEs circularize inefficiently due to weak apsidal precession[34]. For a particularly massive fast-spinning SMBH, efficient circularization is favoured because $R_t \sim R_g$, ensuring large per-orbit precession. The peculiar light curve may also be a natural consequence of tidal disruption by extremely massive black holes. In Methods we combine two competing models (the "circularization"[33] and the "accretion/reprocessing" [35] paradigms) for the optical emission in TDEs and show that the most massive SMBHs produce an unusual hierarchy of tidal disruption timescales. Since the viscous time in the accretion disk is much longer than the debris fallback time when $M_\bullet$ is greater than a few times $10^7 M_\odot$, TDEs around the most massive SMBHs can display an early peak in the light curve from circularization luminosity, and a second peak from reprocessed accretion luminosity.

1. Rees, M. J. Tidal disruption of stars by black holes of 10 to the 6th-10 to the 8th solar masses in nearby galaxies. *Nature* **333**, 523–528 (1988).

2. Hills, J. G. Possible power source of Seyfert galaxies and QSOs. *Nature* **254**, 295–298 (1975).

3. van Velzen, S. *et al.* Optical Discovery of Probable Stellar Tidal Disruption Flares. *Astrophys. J.* **741**, 73 (2011). `1009.1627`.

4. Gezari, S. *et al.* An ultraviolet-optical flare from the tidal disruption of a helium-rich stellar core. *Nature* **485**, 217–220 (2012). `1205.0252`.

5. Arcavi, I. *et al.* A Continuum of H- to He-rich Tidal Disruption Candidates With a Preference for E+A Galaxies. *Astrophys. J.* **793**, 38 (2014). `1405.1415`.

6. Holoien, T. W.-S. *et al.* ASASSN-14ae: a tidal disruption event at 200 Mpc. *Mon. Not. R. Astron. Soc.* **445**, 3263–3277 (2014). `1405.1417`.

7. Dong, S. *et al.* ASASSN-15lh: A highly super-luminous supernova. *Science* **351**, 257–260 (2016). `1507.03010`.

8. Quimby, R. M. *et al.* Hydrogen-poor superluminous stellar explosions. *Nature* **474**, 487–489 (2011). `0910.0059`.

9. Cenko, S. B. *et al.* An Ultraviolet Spectrum of the Tidal Disruption Flare ASASSN-14li. *Astrophys. J. Letters* **818**, L32 (2016). `1601.03331`.

10. Lunnan, R. *et al.* Hydrogen-poor Superluminous Supernovae and Long-duration Gamma-Ray Bursts Have Similar Host Galaxies. *Astrophys. J.* **787**, 138 (2014). `1311.0026`.

11. Leloudas, G. *et al.* Spectroscopy of superluminous supernova host galaxies. A preference of hydrogen-poor events for extreme emission line galaxies. *Mon. Not. R. Astron. Soc.* **449**, 917–932 (2015). 1409.8331.

12. Reines, A. E. & Volonteri, M. Relations between Central Black Hole Mass and Total Galaxy Stellar Mass in the Local Universe. *Astrophys. J.* **813**, 82 (2015). 1508.06274.

13. McConnell, N. J. & Ma, C.-P. Revisiting the Scaling Relations of Black Hole Masses and Host Galaxy Properties. *Astrophys. J.* **764**, 184 (2013). 1211.2816.

14. Kesden, M. Tidal-disruption rate of stars by spinning supermassive black holes. *Phys.R. D* **85**, 024037 (2012). 1109.6329.

15. Mazzali, P. A., Sullivan, M., Pian, E., Greiner, J. & Kann, D. A. Spectrum formation in superluminous supernovae (Type I). *Mon. Not. R. Astron. Soc.* **458**, 3455–3465 (2016). 1603.00388.

16. Strubbe, L. E. & Quataert, E. Spectroscopic signatures of the tidal disruption of stars by massive black holes. *Mon. Not. R. Astron. Soc.* **415**, 168–180 (2011). 1008.4131.

17. Pastorello, A. *et al.* Ultra-bright Optical Transients are Linked with Type Ic Supernovae. *Astrophys. J. Letters* **724**, L16–L21 (2010). 1008.2674.

18. Brown, P. J. *et al.* ASASSN-15lh: A Superluminous Ultraviolet Rebrightening Observed by Swift and Hubble. *Astrophys. J.* **828**, 3 (2016). 1605.03951.

19. de Ugarte Postigo, A. *et al.* The distribution of equivalent widths in long GRB afterglow spectra. *Astron. Astrophys.* **548**, A11 (2012). `1209.0891`.

20. Brown, P. J. Ultraviolet Rebrightening of Superluminous Supernova ASASSN-15lh. *The Astronomer's Telegram* **8086** (2015).

21. Godoy-Rivera, D. *et al.* The Unexpected, Long-Lasting, UV Rebrightening of the Super-Luminous Supernova ASASSN-15lh. *ArXiv e-prints* (2016). `1605.00645`.

22. Inserra, C. *et al.* Super-luminous Type Ic Supernovae: Catching a Magnetar by the Tail. *Astrophys. J.* **770**, 128 (2013). `1304.3320`.

23. Nicholl, M. *et al.* Superluminous supernovae from PESSTO. *Mon. Not. R. Astron. Soc.* **444**, 2096–2113 (2014). `1405.1325`.

24. Chen, T.-W. *et al.* The host galaxy and late-time evolution of the superluminous supernova PTF12dam. *Mon. Not. R. Astron. Soc.* **452**, 1567–1586 (2015). `1409.7728`.

25. Howell, D. A. *et al.* Two Superluminous Supernovae from the Early Universe Discovered by the Supernova Legacy Survey. *Astrophys. J.* **779**, 98 (2013). `1310.0470`.

26. Metzger, B. D., Margalit, B., Kasen, D. & Quataert, E. The diversity of transients from magnetar birth in core collapse supernovae. *Mon. Not. R. Astron. Soc.* **454**, 3311–3316 (2015). `1508.02712`.

27. Sukhbold, T. & Woosley, S. E. The Most Luminous Supernovae. *Astrophys. J. Letters* **820**, L38 (2016). `1602.04865`.

28. Yan, L. *et al.* Detection of Broad Hα Emission Lines in the Late-time Spectra of a Hydrogen-poor Superluminous Supernova. *Astrophys. J.* **814**, 108 (2015). `1508.04420`.

29. Leloudas, G. *et al.* Polarimetry of the Superluminous Supernova LSQ14mo: No Evidence for Significant Deviations from Spherical Symmetry. *Astrophys. J. Letters* **815**, L10 (2015). `1511.04522`.

30. Stone, N. C. & Metzger, B. D. Rates of stellar tidal disruption as probes of the supermassive black hole mass function. *Mon. Not. R. Astron. Soc.* **455**, 859–883 (2016). `1410.7772`.

31. Kochanek, C. S. Tidal disruption event demographics. *Mon. Not. R. Astron. Soc.* **461**, 371–384 (2016). `1601.06787`.

32. Reynolds, C. S. Measuring Black Hole Spin Using X-Ray Reflection Spectroscopy. *Space Science Reviews* **183**, 277–294 (2014). `1302.3260`.

33. Piran, T., Svirski, G., Krolik, J., Cheng, R. M. & Shiokawa, H. Disk Formation Versus Disk Accretion - What Powers Tidal Disruption Events? *Astrophys. J.* **806**, 164 (2015). `1502.05792`.

34. Dai, L., McKinney, J. C. & Miller, M. C. Soft X-Ray Temperature Tidal Disruption Events from Stars on Deep Plunging Orbits. *Astrophys. J. Letters* **812**, L39 (2015). `1507.04333`.

35. Guillochon, J., Manukian, H. & Ramirez-Ruiz, E. PS1-10jh: The Disruption of a Main-sequence Star of Near-solar Composition. *Astrophys. J.* **783**, 23 (2014). `1304.6397`.

Author Contributions   GL coordinated the PESSTO observations, was PI of the FORS2 program, analysed the data and wrote the paper. MF provided the astrometric localisation and reduced the PESSTO spectra. NCS calculated the relation between the BH spin and the Hills mass and edited the manuscript.

SvV performed the *Swift* photometry. PGJ analysed XMM data and helped coordinating the project. IA is the PESSTO PI for TDEs and provided LCOGT data. CF made the LCOGT photometry. JRM reduced the FORS2 spectra. SJS is the PI of PESSTO and helped coordinating the project. TKr provided the SED fit of the host galaxy. JCAMJ provided the radio observations. PMV helped with the analysis of the spectra. GL, MF, NCS, SvV, PGJ, IA, SJS, JCAMJ, AG-Y and PAM contributed to the discussions. AdUP and ADC worked on the UV spectrum. DAH is the PI of the LCOGT observations. CI and OY are PESSTO builders and helped with the analysis. FP, DM, JS and JCW provided FORS2 data and analysis. MC and BET provided the WIFES spectra. SS and SK provided the Magellan spectrum. GH, CMcC and SV obtained and reduced LCOGT data. EK, KM, KWS, MS, and DRY are PESSTO builders and CA, JH, SM, TWC, TKa, SP, CRC, HK, MN, JL, NER, HC, IB, JJ, MRM contributed with PESSTO observations or data reductions. Many authors provided comments on the manuscript.

Competing Interests   The authors declare that they have no competing financial interests.
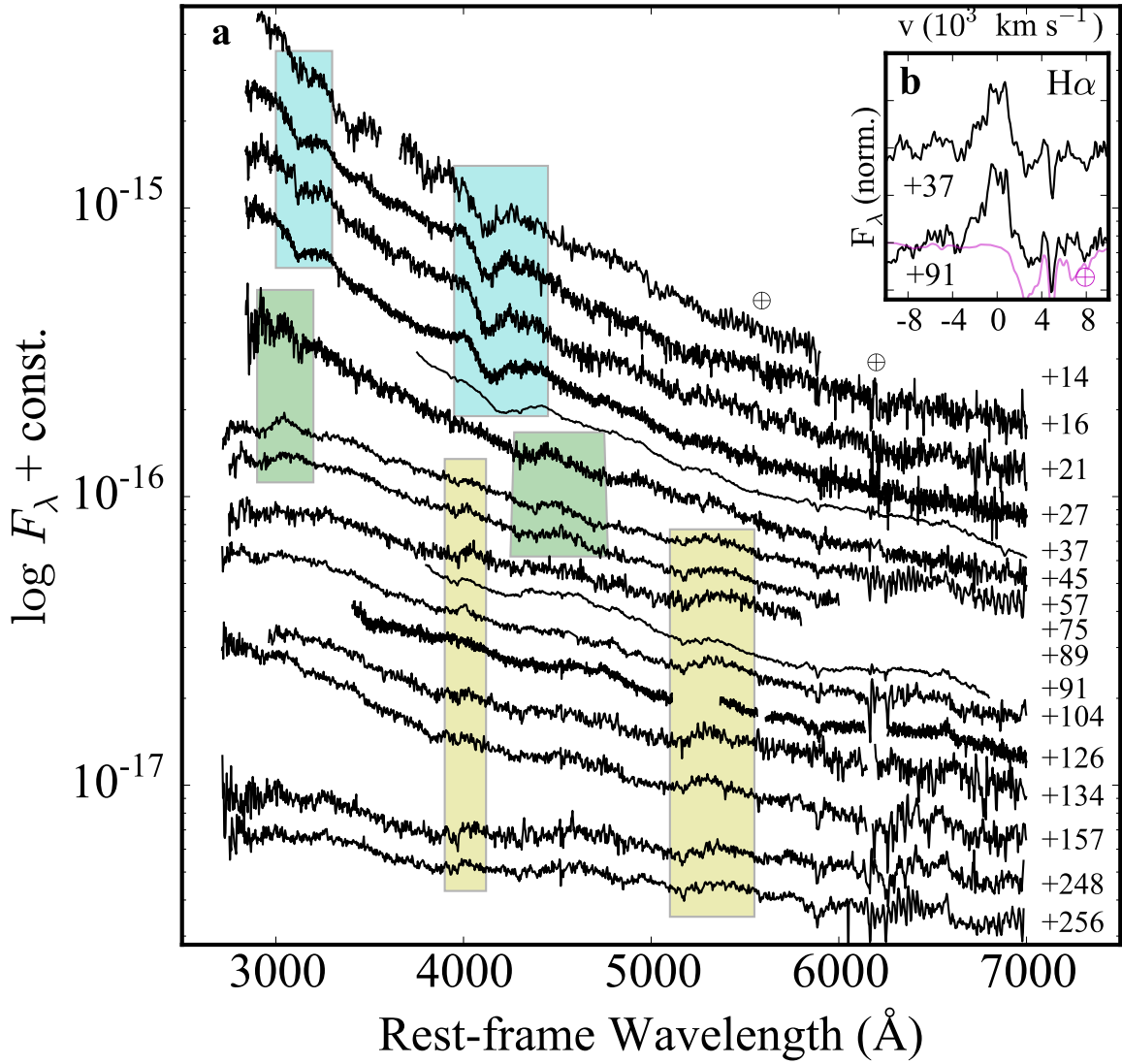
Figure 1 | **Spectral sequence of ASASSN-15lh showing three spectroscopic phases.**

a, The main spectral features during the different phases are highlighted with different colours. The two most recent spectra appear redder due to the increased host contamination. Rest-frame phases are indicated, the spectra have been offset for clarity and the Earth symbol marks the strongest telluric features. **b,** Detection of $H\alpha$ (FWHM $\sim 2,500$ km

17

s^{-1}) in a telluric-free region of our best spectra. The magenta line is a telluric spectrum.
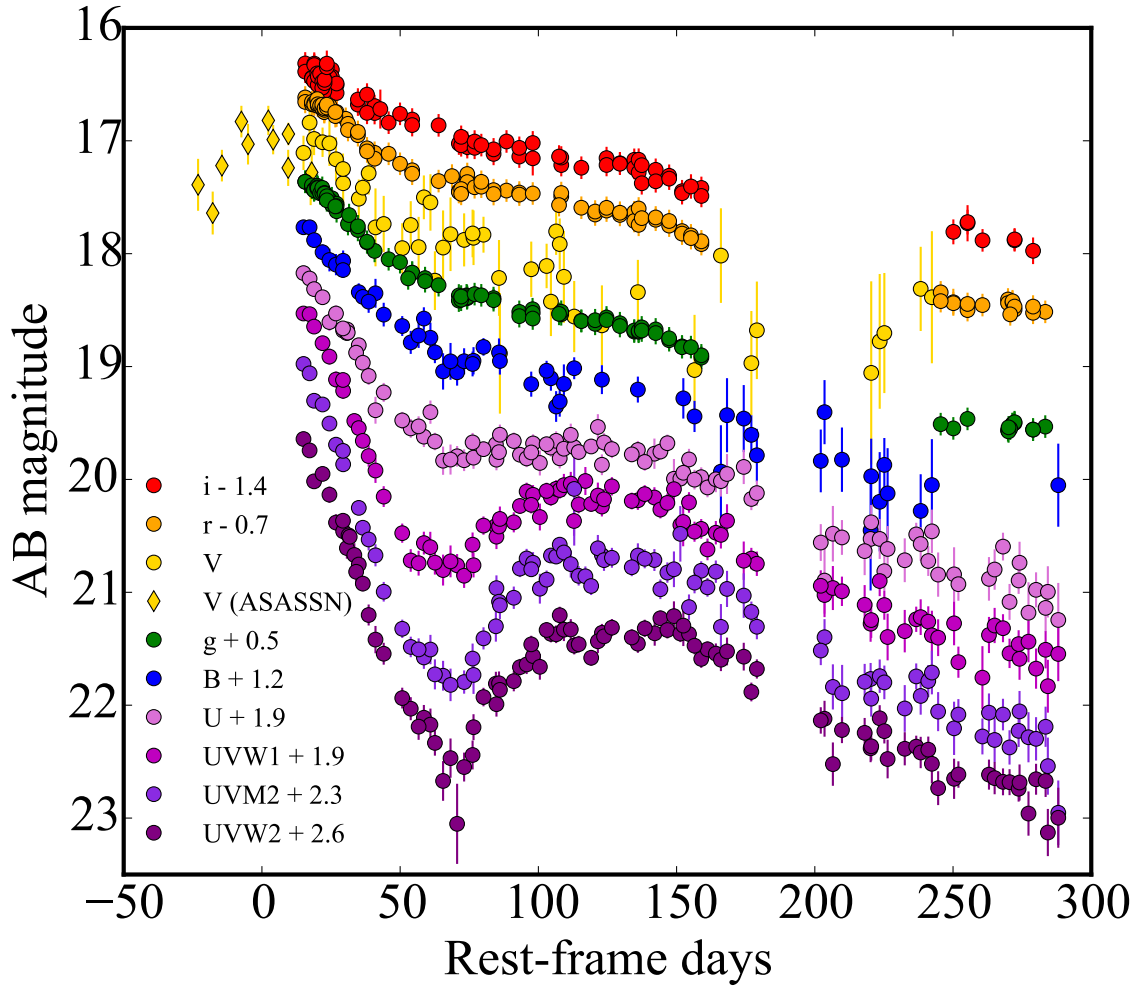
Figure 2 | **The light curve evolution of ASASSN-15lh in the rest frame.** The data are from LCOGT (gri) and *Swift* (other filters), supplemented by the ASASSN V-band data[7]. We have adopted a peak time at 5 June 2015 (MJD 57178.5)[7]. The light curves are shifted for clarity as indicated in the legend. Error bars represent 1σ uncertainties. The optical bands show a monotonic decline, but the UV bands show a rebrightening after 60 rest-frame days. A significant secondary dip is also observed in the bluest bands

19

around day +120. The photometry has been corrected for foreground extinction and the

host contribution has been removed (see Methods).
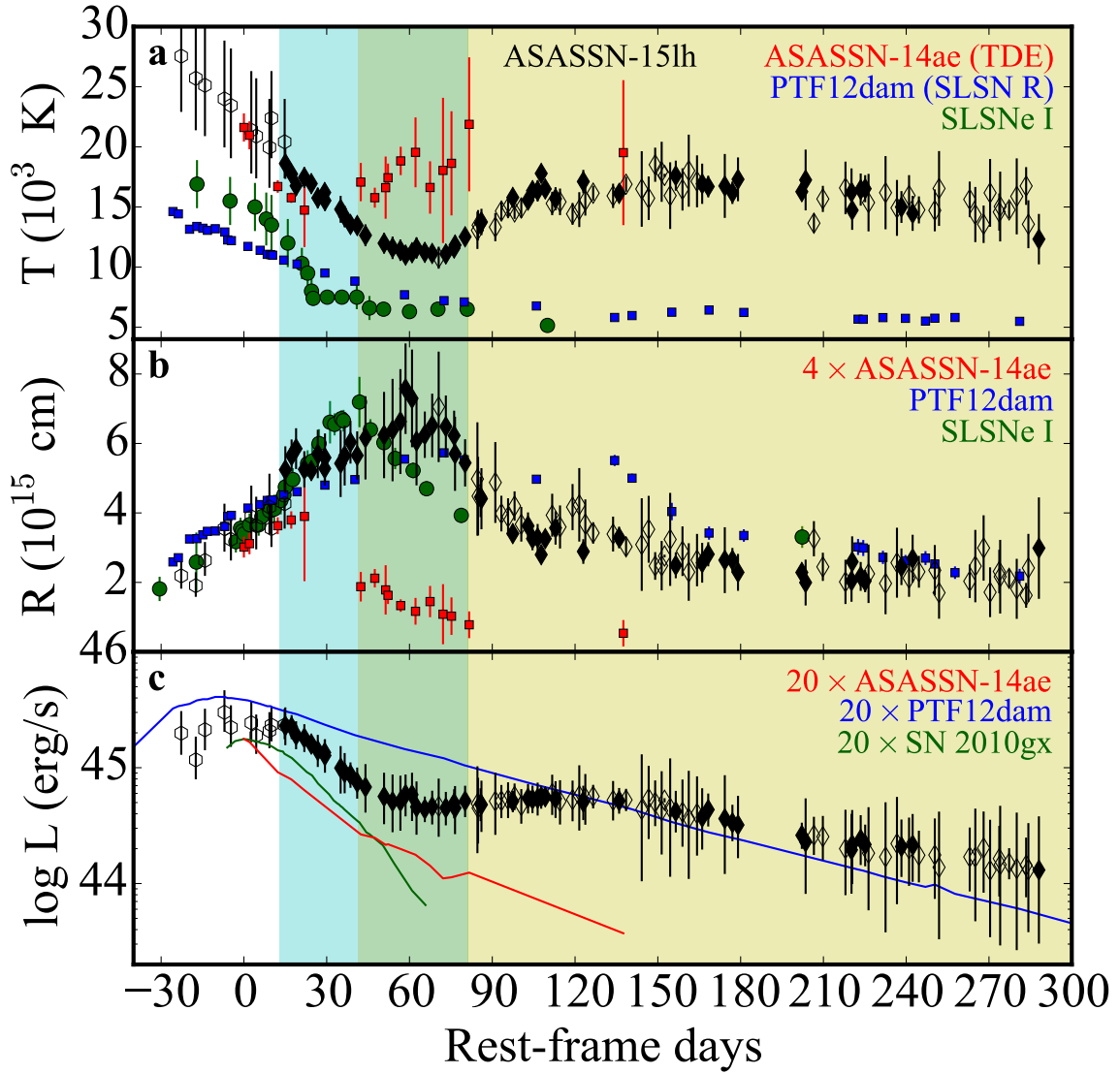
Figure 3 | **The evolution of the temperature, radius and luminosity of ASASSN-15lh, compared with TDEs[6] and SLSNe[17, 22, 23, 24]**. The coloured areas correspond to the different spectroscopic phases in Figure 1. For ASASSN-15lh (data in black), open symbols show fits based on fewer than five filters. In particular, open hexagon symbols show early data, based only on the V band and derived with a temperature prior[7]. Error

21

bars represent 1σ uncertainties. The curves are shown with respect to peak time and some comparison objects have been scaled as indicated in the legend. **a,b,** The evolution of the temperature **(a)** and radius **(b)** of ASASSN-15lh are qualitatively similar to those of the TDE ASASSN-14ae, although this is happening in longer timescales and larger radii. All types of SLSNe cool down with time. **c,** The bolometric luminosity of ASASSN-15lh shows an extended plateau between 70 and 160 days.
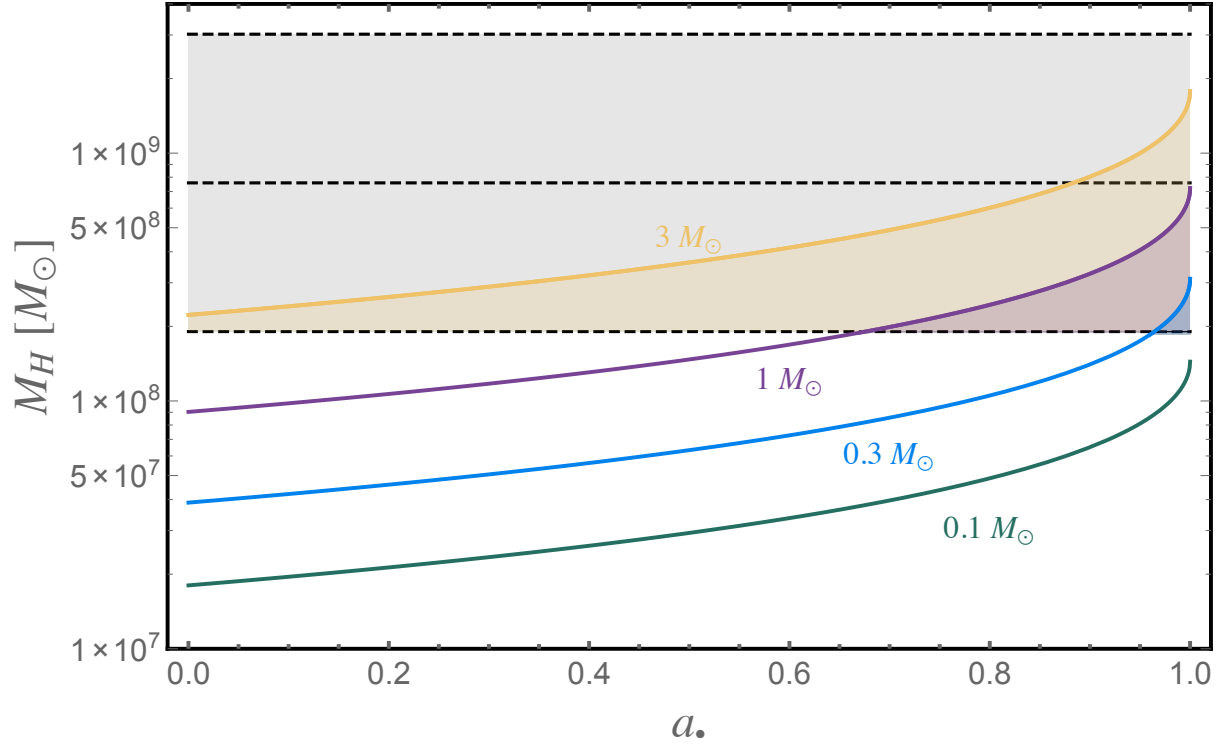
Figure 4 | **The Hills mass M_{H} as a function of SMBH spin $a_{\bullet}$ for main sequence stars of different masses.** The SMBH mass estimate[12] for the host of ASASSN-15lh and the corresponding 1σ uncertainty region are shown as dashed lines and grey shading. The plot shows that a star of mass $0.1M_{\odot}$ cannot be disrupted by the SMBH, as the Hills mass is always below the mass of the SMBH. Stars of mass $0.3M_{\odot}$ and $1M_{\odot}$ can be disrupted by rotating Kerr black holes of different spins. Only stars of mass $3M_{\odot}$ lie in the allowed region for TDEs from a non-rotating Schwarzschild black hole, but TDEs from such stars are unlikely[30, 31].

Methods

We describe here the data, methods and theoretical calculations used. We provide details on the localization of ASASSN-15lh and on the host galaxy properties. We present the different data used, and describe the reductions and comment on the implications. Finally, we demonstrate that a TDE can easily accommodate the luminosity and energetics of ASASSN-15lh, we show that combining two luminosity mechanisms for TDEs can result in light curves with two different timescales and we present our derivation of the relativistic Hills mass as a function of the SMBH spin. We assume a *Planck* cosmology[36].

Astrometric localisation of ASASSN-15lh *HST* observations of ASASSN-15lh were obtained under programme 14348 (PI: Yang) with ACS and a broad-band polarimetry filter (POL0V) and the F606W filter. All analyses were performed on the reduced drizzled image obtained from the MAST archive. The image was taken on 2015 August 3, and the total exposure time for this frame was 366 s. The DECam image was a 90 s image taken on 2014 October 22 using an r-band filter. The DECam data were reduced using the DES Data Management Pipeline and are available online[37]. The measured FWHM was $0.8''$.

Eight sources common to both the DECam and ACS images were used to derive a geometric transformation (allowing for rotation, translation and a single scaling factor) between the two frames. Of these sources, five were unresolved in the ACS image and the remaining three had a FWHM of less than about twice that of the point sources. The root mean square error error in the transformation was 0.19 DECam pixels, or 52 mas. To measure the position of the host galaxy in

the DECam frame, we fitted a model galaxy profile using the GALFIT code; uncertainties in the galaxy centroid were estimated to be only a few $\times 0.01$ pixels from Monte Carlo tests. The position of ASASSN-15lh on the ACS image yields an accuracy of 0.05 pixels (or 3 mas) using three different centering algorithms within the IRAF PHOT package.

The host galaxy To derive the physical properties of the host galaxy of ASASSN-15lh through modeling of its spectral energy distribution (SED), we used $grizY$ [37], J and $K_{\rm s}$ [38], as well as $3.4\,\mu$m and $4.6\,\mu$m *WISE* photometry. We also performed aperture photometry on *GALEX* images yielding no significant detections.

We fitted the Galactic extinction-corrected[39] photometry of the host with stellar population synthesis models[40] using the code *Le Phare*[41, 42]. Our galaxy templates were based on a Chabrier initial mass function[43], and spanned different stellar metallicities, e-folding timescales τ (0.1 to 30 Gyr), stellar population ages (0.01 to 10 Gyr) and dust attenuations[44]. The galaxy stellar mass and SFR are $\log_{10} M_\star = 10.95^{+0.15}_{-0.11}$ M$_\odot$ and $0.05^{+0.15}_{-0.05}$ M$_\odot$ yr^{-1}, respectively. Physical parameters are given as the median of the probability distribution of all templates, with error-bars containing the 1σ probability interval. The best fit model is shown in Supplementary Figure 6 and it has a low $E(B-V)_{\rm host} = 0.02$ mag. Throughout the paper, we assume that the extinction at the host is negligible.

We also constrain the recent star formation in the host by placing limits on the flux of [O II] and (narrow) Hα. Using the FORS2 spectra (signal-to-noise ratio > 200) we obtain flux limits of $< 1.8 \times 10^{-16}$ erg s^{-1} cm^{-2} for [O II] and $< 2.9 \times 10^{-17}$ erg s^{-1} cm^{-2} for Hα (2σ). These limits

constrain the SFR to < 0.25 and < 0.02 M$_\odot$ yr^{-1} respectively[45, 43], an improvement by a factor of ten over previous estimates[7].

***HST* UV spectroscopy** A UV spectrum of ASASSN-15lh was obtained on day $+168$ with *HST* under program 14450 (PI: Brown). We downloaded the reduced COS and STIS spectra from the MAST archive. The spectrum does not display any broad emission or absorption features (at similar phases the optical spectrum is also mostly featureless; Figure 1). We identified both geocoronal and absorption lines at $z = 0$ and a number of narrow (FWHM $\sim 200 - 400$ km s^{-1}) absorption features at the redshift of ASASSN-15lh. Supplementary Figure 4 shows the COS spectrum (the STIS spectrum is more noisy and less interesting). Supplementary Table 1 contains the EWs and kinematical offsets (measured relative to Ly-α) for lines that were detected, as well as selected limits.

Low-ionisation features, such as Fe II and Si II, which are common in the star-forming sight-lines of SLSNe[46] or GRBs[47, 19] are weak or absent in ASASSN-15lh. In contrast, absorption from high ionisation lines from N V and O VI is remarkably strong, especially relatively to the (weak) Ly-α. In particular, the ratio of N V to Ly-α is $\sim$4, while it is $>$1,000 lower in GRBs. The same is true for column densities: by Voigt profile modelling, we derived $N(H\ I) = 14.73 \pm 0.12$, $N(O\ VI) = 15.58 \pm 0.03$, $N(N\ V) = 15.42 \pm 0.06$ and $N(C\ IV) = 14.60 \pm 0.27$, resulting in ratios that are highly unusual for GRB or Quasar DLAs[48, 49], even if those values are lower limits due to saturation. The ratio of N V to Ly-α was also observed to be of the order of unity in the spectrum of ASASSN-14li, the only UV spectrum of a TDE[9]. By complementing our measurements with those from optical spectra[7], we found that the Mg II absorption is weak, below the value for GRBs[47, 19]

and SLSNe[46].

Therefore we suggest that the absorbing gas can be separated into two components: (1) a tenuous mildly-ionised medium (Ly-α, Mg II, Si III at velocities from 0 to +44 km s^{-1}), which is very unusual given the lack of Fe II and Si II, and (2) a highly-ionised medium (N V, O VI and C IV) at negative velocity offsets -80 to -120 km s^{-1}. We suggest that the latter is consistent with material from a disrupted low-mass star[50, 9] and that it is ionised by the TDE. Despite the absence of broad features, the phenomenological similarity with the UV spectrum of ASASSN-14li strongly favours a TDE origin for ASASSN-15lh. A highly-ionised outflow was also detected for ASASSN-14li in X-rays[51].

Optical spectroscopy Spectra were obtained with the instruments and set-ups listed in Supplementary Table 2. The FLOYDS, WiFeS and EFOSC2 data were reduced using dedicated instrument pipelines [52, 53, 54]. The VLT+FORS2 and Magellan+IMACS spectra were reduced in the standard fashion using IRAF. The FORS2 spectra were obtained in spectropolarimetric mode, but the ordinary and extraordinary rays were combined to produce an intensity spectrum.

Imaging and removal of the host contribution The LCOGT gri images were pre-processed using the Observatory Reduction and Acquisition Control Data Reduction pipeline[55]. To remove the host contribution, we performed image subtraction using the pre-discovery DECam gri images as templates. The *Swift* UVOT observations were reduced following the standard procedures and software (UVOTSOURCE). To extract the photometry, we used a $4''$ aperture and a curve of growth aperture correction. For the *Swift* filters we did not have pre-discovery observations, and hence

used the model galaxy spectrum from the SED fit (Supplementary Figure 6) to generate synthetic magnitudes at these wavelengths. For the B and V filters, where host contamination is a concern, we estimated the host uncertainty to be < 0.05 mag, increasing to 0.1 mag for the U band. The host uncertainties in the UV filters are more significant, but at these wavelengths the host is many orders of magnitude below the transient luminosity. In the AB system we obtained host magnitudes of $V = 18.98, B = 20.43, U = 21.95, UVW1 = 23.21, UVM2 = 23.65$ and $UVW2 = 23.62$ mag, which we subtracted from the *Swift* measurements to obtain the transient photometry. Two UVOT filters suffer from a red leak but this does not affect blue sources as ASASSN-15lh to the same degree as e.g. SNe Ia[56]. Based on synthetic photometry of black-body spectra, we estimated that the photometry is affected by $< 2\%$ for a black body with $T = 15,000$ K. As this precision is significantly lower than our photometric accuracy, we did not attempt to correct for this effect. Another study[18] has found higher values – but still low – for this maximum contamination.

Radio and X-ray observations We observed ASASSN-15lh from 05:00 to 14:00 UT on 9 December 2015, using the Australia Telescope Compact Array in 750C configuration, under project code CX340. We observed in two frequency bands of width 2.048 GHz, centered at 5.5 and 9.0 GHz. We used B1934-638 as both our flux and bandpass calibrator, and B2205-636 as our phase calibrator. We reduced the data following standard procedures in Miriad[57], and carried out the imaging and self-calibration using the Common Astronomy Software Application[58].

The field was dominated by PKS J2203-6130, a 9-mJy source (prior to primary beam correction) located 15 arcmin away from the target. We performed self-calibration, initially in phase only (down to a timescale of 2 min), and eventually in amplitude and phase, on a timescale of 10 min.

Given the non-uniform *uv*-coverage, we tested a variety of image weighting schemes, and found the optimum to be a Briggs robust weighting of 0.5. ASASSN-15lh was not detected down to 3σ upper limits of 25 and 23 μJy beam^{-1} at 5.5 and 9.0 GHz, respectively, consistent with a reported upper limit from three weeks earlier[59]. Stacking our two frequency bands gave us a slightly deeper 3σ radio upper limit of 17 μJy beam^{-1}.

The XMM–*Newton* satellite observed ASASSN–15lh as part of a Directors Discretionary Time proposal on 18 November 2015. The on–source time is 11.9 ks, and after filtering epochs of high background, 9 ks of MOS2, and 4 ks of PN data can be used. Given the lower background and the longer net exposure, we used the MOS2 detector for estimating the upper limit on the source flux. In an aperture of radius 32" centred on ASASSN-15lh we derived a 95% confidence upper limit[60, 61] of 11 source counts in the 0.15–1 keV band. To convert this to a limit on the flux, we use a temperature of 70 eV found for ASASSN–14li as input, which taking into account that the $M_\bullet$ in ASASSN–15lh is close to 8×10^8 $M_\odot$, and that of ASASSN–14li is closer to 2×10^6 $M_\odot$, implies a blackbody temperature of 18 eV (as $T \propto M^{-0.25}$). With this and N_H=3×20 cm^{-2} W3PIMMS provides a 95% upper limit to the 0.3–1 keV X–ray flux of 2×10^{-16} erg cm^{-2} s^{-1}, yielding an upper limit to the source luminosity of 3×10^{40} erg s^{-1}. This limit depends strongly on the chosen energy band. The 0.3–1 keV band was chosen to allow comparison with ASASSN-14li[62].

If TDEs do in fact all produce radio jets, as suggested by the recent detection of ASASSN-14li[62], then applying the same model with appropriate scalings would predict a radio flux of 10 μJy at the time of the observations. The fact that we did not detect a radio jet therefore remains consistent with a TDE origin for ASASSN-15lh, and implies that the jet power of ASASSN-15lh

is $\nu L_\nu \lesssim 10^{38}$ erg s^{-1}, which is at least 2-3 orders of magnitude lower than that of the relativistic TDE Swift J1644+57[63]. This difference was probably caused by a combination of misalignment of the jet axis and the line of sight (consistent with our non-detection of X-ray) and differences in accretion flow geometry, interstellar medium density or magnetic field strength[64]. If black hole spin were the dominant factor in setting jet power, we would have expected ASASSN-15lh to host a jet at least comparable in strength to ASASSN-14li (as we have inferred a high black hole spin for ASASSN-15lh). Given that our upper limit is close to the ASASSN-14li model prediction, this jet should have been detectable unless the spin of ASASSN-15lh is significantly less than we have inferred, the ISM density is extremely low, or the SMBH in ASASSN-14li is also rapidly spinning.

Tidal Disruption Luminosities and Energetics In Newtonian theory, a star with mass $M_\star \equiv m_\star M_\odot$ and radius $R_\star \equiv r_\star R_\odot$ will be tidally disrupted when it approaches an SMBH of mass $M_\bullet \equiv M_8 10^8 M_\odot$ within a distance:

$$R_\mathrm{t} = R_\star \left(\frac{M_\bullet}{M_\star} \right)^{1/3} \tag{1}$$

Stars passing within this tidal radius can create a luminous electromagnetic flare provided $R_\mathrm{t} \gtrsim R_\mathrm{IBCO}$, the location of the innermost bound circular orbit (IBCO) for the SMBH. This occurs for SMBHs smaller than the Hills mass[2],

$$M_\mathrm{H} \equiv 9 \times 10^7 M_\odot r_\star^{3/2} m_\star^{-1/2} \tag{2}$$

Once the star has been disrupted, half of its gas is unbound from the SMBH; the other half remains bound with a characteristic spread in specific orbital energy [65, 66]

$$\Delta\epsilon = \frac{G M_\bullet R_\star}{R_\mathrm{t}^2} \tag{3}$$

If we assume a top-hat distribution of debris energy, then the fallback time (in units of seconds) for the most tightly bound debris is

$$t_{\mathrm{f}} = 3.5 \times 10^7 \ M_8^{1/2} m_\star^{-1} r_\star^{3/2} \tag{4}$$

which gives a peak fallback rate

$$\frac{\dot{M}_{\mathrm{p}}}{\dot{M}_{\mathrm{Edd}}} = 0.13 \eta_{-1} M_8^{-3/2} m_\star^2 r_\star^{-3/2} \tag{5}$$

where $\eta = 0.1 \eta_{-1}$ is the radiative efficiency of accretion used to calculate the Eddington-limited mass inflow rate $\dot{M}_{\mathrm{Edd}}$. The peak bolometric luminosity is

$$L_{\mathrm{p}} = 1.9 \times 10^{45} \eta_{-1} M_8^{-1/2} m_\star^2 r_\star^{-3/2} \ \mathrm{erg \ s}^{-1} \tag{6}$$

which is easily compatible with our observations for $m_\star = 1$ and $\eta = 0.42$, appropriate for Kerr black holes. The radiated bolometric energy is

$$E_{\mathrm{rad}} = 8.9 \times 10^{52} \ \eta_{-1} m_\star \ \mathrm{erg} \tag{7}$$

ASASSN-15lh, although extreme as a SN [26, 27, 67, 68, 69], does not strain the theoretical luminosity or energy budgets of TDEs.

Tidal Disruption Flare Timescales Existing observations do not yet distinguish between two competing theories for producing TDE optical emission. In the accretion/reprocessing paradigm, the bolometric luminosity of a compact ($\sim 10 R_{\mathrm{g}}$), efficiently circularized accretion disk is intercepted by an optically thick screen of gas at larger scales ($\sim 10^3 R_{\mathrm{g}}$). This reprocessing layer may be a slow outflow from the disk [70], or a more hydrostatic configuration [71, 35, 72]. However,

in both cases it absorbs and re-emits a large fraction of the disk bolometric luminosity at longer

wavelengths. Both cases predict a larger reprocessing layer for larger SMBHs: outflow velocities

$v_{\rm w} \sim \sqrt{GM_\bullet/R_{\rm t}} \propto M_\bullet^{1/3}$, or, if we assume that a hydrostatic reprocessing layer exists at scales

comparable to the semimajor axis of the most tightly bound material, its size is proportional to

$M_\bullet^{2/3}$. Alternatively, in the circularization paradigm, observed optical emission arises from shocks

between debris streams[33], which thermalize and radiate stream kinetic energy at the (generally

large) stream self-intersection radius.

The efficiency of circularization (and therefore $\dot{M}_{\rm p}$) depends sensitively on the dimensionless

orbital pericenter $R_{\rm p}/R_{\rm g}$: small decreases in $R_{\rm p}$ quickly move the self-intersection point inward,

increasing circularization efficiency [73, 74]. The low luminosities seen in many optically-selected

TDEs may reflect that most TDEs have sub-relativistic pericenters and circularize inefficiently, so

that their peak luminosity is $\ll \eta\dot{M}_{\rm p}c^2$ [34].

For an extremely massive SMBH with $M_\bullet \approx M_{\rm H}$, all TDE pericenters are highly relativistic

and circularization is maximally efficient (except possibly if the SMBH spin is rapid and strongly

misaligned[75, 76]). Stream self-intersection points will be $\sim R_{\rm p}$, near the IBCO [34], so the circular-

ization and accretion power will be comparable. It is therefore natural to expect that TDEs from

the most massive SMBHs will be brighter and able to attain their theoretical peak luminosity, while

smaller SMBHs will often produce TDEs that (due to inefficient circularization) have luminosities

well below the peak theoretical luminosity.

We propose that the two peaks in the ASASSN-15lh light curve correspond to two different

32

energy sources: the circularization luminosity, and the accretion luminosity. The former evolves on the fallback timescale t_f while the latter evolves on a viscous timescale,

$$t_v = \sqrt{\frac{8R_p^3}{GM_\bullet}}\alpha^{-1}\left[\frac{H(2R_p)}{2R_p}\right]^{-2} \tag{8}$$

where we have assumed that the disk outer edge is $2R_p$, $\alpha < 1$ is the usual Shakura-Sunyaev viscosity parameter, and H/R is the disk aspect ratio. For standard TDEs, these two sources of luminosity are difficult to disentangle, because $t_v \ll t_f$ [77, 78]: as soon as matter circularizes into a disk, it drains rapidly into the SMBH, and the two sources of luminosity rise and fall together.

However, for very massive SMBHs, $\dot{M}_p < \dot{M}_{Edd}$ and the accretion disk will be geometrically thin, dramatically increasing t_v and producing an inverted timescale hierarchy: $t_v \gtrsim t_f$. The circularization luminosity can be released promptly, but accretion luminosity will be bottlenecked by the long t_v. The range of inferred SMBH masses for ASASSN-15lh yield $\dot{M}_p \lesssim \dot{M}_{Edd}$ (unlike for most other TDE hosts), so it is natural to expect two power sources - circularization and accretion - to have two different peaks.

The characteristic decay time of the first peak will be $\sim t_f$, while that of the second will be t_v, which is a sensitive function of α and H/R. Plausible parameter choices (e.g. $M_\bullet = 10^8 M_\odot$, $\alpha = 0.1$, $H/R = 0.03$) give $t_v \sim 6$ months, in agreement with the observed second component of the light curve. However, the first component of the light curve decays on a timescale of $\sim 1 - 2$ month, unlike the Newtonian estimate of equation 4: $t_f \approx 1$ yr. In the following subsection, we argue that general relativity effects can increase $\Delta\epsilon$ in TDEs with extremely relativistic pericenters, substantially reducing t_f for this subset of TDEs.

Relativistic Alterations to the Fallback Time Highly relativistic tidal disruption will alter the Newtonian $\Delta\epsilon$. The frozen-in energy spread $\Delta\epsilon$ can increase by a factor up to $\sqrt{2}$ (ref. [79]), decreasing t_f and increasing $\dot{M}_\mathrm{p}$ modestly. However, $\Delta\epsilon$ may increase further by modest spin-orbit misalignments in a TDE for sufficiently relativistic pericenters [66]. Here, we argue that this effect can strongly reduce the fallback time from the Newtonian estimate of equation 4.

The extremity of a TDE is quantified not just by $B \equiv R_\mathrm{p}/R_\mathrm{g}$, but also by the penetration factor $\beta \equiv R_\mathrm{t}/R_\mathrm{p}$. TDEs with a large β will strongly compress the star orthogonal to the orbital plane, causing a vertical collapse with velocity $v_\mathrm{z} \approx \beta\sqrt{GM_\star/R_\star}$. The collapse is reversed near pericenter, once internal pressure in the disrupted star builds up to the point where it "bounces" along this vertical axis[80], receiving an almost impulsive hydrodynamic kick $\approx v_\mathrm{z}$ along the direction of collapse. The bounce typically has little effect on the energy spread of the debris[65, 73], despite the fact that $V_\mathrm{p}v_\mathrm{z} \gtrsim \Delta\epsilon$ for large β or small B (here V_p is the orbital velocity at pericenter). One could define a hydrodynamic component of the energy spread, $\Delta\epsilon_\mathrm{h} \equiv \vec{V_\mathrm{p}} \cdot \vec{v}_\mathrm{z} = V_\mathrm{p}v_\mathrm{z}\cos\theta$, but in standard TDEs the misalignment angle $\theta = \pi/2$.

However, for very low B, modest spin-orbit misalignment will precess the orbital plane as the star passes through the tidal sphere, partially aligning the axis of vertical collapse with the orbital velocity vector. The per-orbit precession in the line of ascending nodes for a parabolic orbit is[81]:

$$\delta\Omega = \sqrt{2}\pi a_\bullet \left(\frac{R_\mathrm{g}}{R_\mathrm{p}}\right)^{3/2} \tag{9}$$

at leading post-Newtonian order. Since most of this shift occurs near pericenter, we approximate the rotation in the line of ascending nodes between R_t and the bounce (near R_p) as $\delta\Omega/2$. The

misalignment angle is θ ($\cos\theta \approx \frac{\delta\Omega}{2}\sin I$), where I is the misalignment between spin and orbital angular momentum. Defining a total energy spread $\Delta\epsilon_{\text{tot}} \equiv \Delta\epsilon + \Delta\epsilon_{\text{h}}$, we find (Stone, Kennon, & Metzger, manuscript in preparation):

$$\Delta\epsilon_{\text{tot}} = \Delta\epsilon(1 + a_\bullet\beta^{3/2}B^{-3/2}\sin I) \tag{10}$$

The above arguments are approximate, as the post-Newtonian approximation begins to break down for $R_{\text{p}} \sim R_{\text{g}}$, and we have treated the bounce hydrodynamics impulsively. A detailed examination of this spin-orbit coupling is beyond the scope of this paper, but order unity increases in $\Delta\epsilon$ and decreases in $t_{\text{f}} \propto \Delta\epsilon^{3/2}$ are expected for TDEs around SMBHs with $a_\bullet \approx 1$ and $B \sim 1$.

Relativistic Calculation of the Hills Mass Some of the previous Newtonian estimates break down when the star's orbital pericenter $R_{\text{p}} \sim R_{\text{g}}$. In this regime, general relativistic effects are crucial for proper modelling of the Hills mass[82, 14]. The increased M_{H} arises from two different effects: first, a large $a_\bullet$ will lower the IBCO radius significantly, and second, the Kerr tidal field is somewhat stronger than the Schwarzschild equivalent.

To calculate $M_{\text{H}}(a_\bullet)$, we employ Fermi normal coordinates to write a local, fully general relativistic tidal tensor[83]. We then employ the accepted formalism[14] to estimate relativistic Hills masses. The results are shown for equatorial orbits (that maximize M_{H}) in Figure 4, where we see that the relativistic Kerr M_{H} can be almost an order of magnitude greater than the Newtonian (or Schwarzschild) equivalent.

Data Availability Statement The photometry and spectra of ASASSN-15lh supporting the findings of this study are available from WISeREP[84] ($http://wiserep.weizmann.ac.il/$)

36. Planck Collaboration XVI. Planck 2013 results. XVI. Cosmological parameters. *Astron. Astrophys.* **571**, A16 (2014). `1303.5076`.

37. Melchior, P. *et al.* Optical broad-band photometry and reference image for APMUKS(BJ) B215839.70-615403.9 / ASASSN-15lh from the Dark Energy Survey. *The Astronomer's Telegram* **7843** (2015).

38. Prieto, J. L. *et al.* APMUKS(BJ) B215839.70-615403.9: The massive host galaxy candidate of ASASSN-15lh. *The Astronomer's Telegram* **7776** (2015).

39. Schlafly, E. F. & Finkbeiner, D. P. Measuring Reddening with Sloan Digital Sky Survey Stellar Spectra and Recalibrating SFD. *Astrophys. J.* **737**, 103 (2011). `1012.4804`.

40. Bruzual, G. & Charlot, S. Stellar population synthesis at the resolution of 2003. *Mon. Not. R. Astron. Soc.* **344**, 1000–1028 (2003). `astro-ph/0309134`.

41. Arnouts, S. *et al.* Measuring and modelling the redshift evolution of clustering: the Hubble Deep Field North. *Mon. Not. R. Astron. Soc.* **310**, 540–556 (1999). `astro-ph/9902290`.

42. Ilbert, O. *et al.* Accurate photometric redshifts for the CFHT legacy survey calibrated using the VIMOS VLT deep survey. *Astron. Astrophys.* **457**, 841–856 (2006). `astro-ph/0603217`.

43. Chabrier, G. Galactic Stellar and Substellar Initial Mass Function. *Publications of the Astronomical Society of the Pacific* **115**, 763–795 (2003). `astro-ph/0304382`.

44. Calzetti, D. *et al.* The Dust Content and Opacity of Actively Star-forming Galaxies. *Astrophys. J.* **533**, 682–695 (2000). `astro-ph/9911459`.

45. Kennicutt, R. C., Jr. Star Formation in Galaxies Along the Hubble Sequence. *Ann. Rev. Astron. Astrophys.* **36**, 189–232 (1998). `astro-ph/9807187`.

46. Vreeswijk, P. M. *et al.* The Hydrogen-poor Superluminous Supernova iPTF 13ajg and its Host Galaxy in Absorption and Emission. *Astrophys. J.* **797**, 24 (2014). `1409.8287`.

47. Christensen, L. *et al.* A High Signal-to-noise Ratio Composite Spectrum of Gamma-ray Burst Afterglows. *Astrophys. J.* **727**, 73 (2011). `1011.0734`.

48. Fox, A. J., Petitjean, P., Ledoux, C. & Srianand, R. Hot halos around high redshift proto-galaxies. Observations of O VI and N V absorption in damped Lyman-α systems. *Astron. Astrophys.* **465**, 171–184 (2007). `astro-ph/0701392`.

49. Fox, A. J., Ledoux, C., Vreeswijk, P. M., Smette, A. & Jaunsen, A. O. High-ion absorption in seven GRB host galaxies at z = 2-4. Evidence for both circumburst plasma and outflowing interstellar gas. *Astron. Astrophys.* **491**, 189–207 (2008). `0809.3247`.

50. Kochanek, C. S. Abundance anomalies in tidal disruption events. *Mon. Not. R. Astron. Soc.* **458**, 127–134 (2016). `1512.03065`.

51. Miller, J. M. *et al.* Flows of X-ray gas reveal the disruption of a star by a massive black hole. *Nature* **526**, 542–545 (2015). `1510.06348`.

52. Dopita, M. *et al.* The Wide Field Spectrograph (WiFeS). *Ap&SS* **310**, 255–268 (2007). `0705.0287`.

53. Dopita, M. *et al.* The Wide Field Spectrograph (WiFeS): performance and data reduction. *Ap&SS* **327**, 245–257 (2010). `1002.4472`.

54. Smartt, S. J. *et al.* PESSTO: survey description and products from the first data release by the Public ESO Spectroscopic Survey of Transient Objects. *Astron. Astrophys.* **579**, A40 (2015). `1411.0299`.

55. Jenness, T. & Economou, F. ORAC-DR: A generic data reduction pipeline infrastructure. *Astronomy and Computing* **9**, 40–48 (2015). `1410.7509`.

56. Brown, P. J. *et al.* The Absolute Magnitudes of Type Ia Supernovae in the Ultraviolet. *Astrophys. J.* **721**, 1608–1626 (2010). `1007.4842`.

57. Sault, R. J., Teuben, P. J. & Wright, M. C. H. A Retrospective View of MIRIAD. In Shaw, R. A., Payne, H. E. & Hayes, J. J. E. (eds.) *Astronomical Data Analysis Software and Systems IV*, vol. 77 of *Astronomical Society of the Pacific Conference Series*, 433 (1995). `astro-ph/0612759`.

58. McMullin, J. P., Waters, B., Schiebel, D., Young, W. & Golap, K. CASA Architecture and Applications. In Shaw, R. A., Hill, F. & Bell, D. J. (eds.) *Astronomical Data Analysis Software and Systems XVI*, vol. 376 of *Astronomical Society of the Pacific Conference Series*, 127 (2007).

59. Kool, E. C. *et al.* Radio Non-Detection of ASASSN-15lh = SN2015L. *The Astronomer's Telegram* **8388** (2015).

60. Kraft, R. P., Burrows, D. N. & Nousek, J. A. Determination of confidence limits for experiments with low numbers of counts. *Astrophys. J.* **374**, 344–355 (1991).

61. Helene, O. Errors in experiments with small numbers of events. *Nuclear Instruments and Methods in Physics Research A* **228**, 120–128 (1984).

62. van Velzen, S. *et al.* A radio jet from the optical and x-ray bright stellar tidal disruption flare ASASSN-14li. *Science* **351**, 62–65 (2016). `1511.08803`.

63. Levan, A. J. *et al.* An Extremely Luminous Panchromatic Outburst from the Nucleus of a Distant Galaxy. *Science* **333**, 199 (2011). `1104.3356`.

64. Tchekhovskoy, A., Metzger, B. D., Giannios, D. & Kelley, L. Z. Swift J1644+57 gone MAD: the case for dynamically important magnetic flux threading the black hole in a jetted tidal disruption event. *Mon. Not. R. Astron. Soc.* **437**, 2744–2760 (2014). `1301.1982`.

65. Guillochon, J. & Ramirez-Ruiz, E. Hydrodynamical Simulations to Determine the Feeding Rate of Black Holes by the Tidal Disruption of Stars: The Importance of the Impact Parameter and Stellar Structure. *Astrophys. J.* **767**, 25 (2013). `1206.2350`.

66. Stone, N., Sari, R. & Loeb, A. Consequences of strong compression in tidal disruption events. *Mon. Not. R. Astron. Soc.* **435**, 1809–1824 (2013). `1210.3374`.

67. Bersten, M. C., Benvenuto, O. G., Orellana, M. & Nomoto, K. The Unusual Super-luminous Supernovae SN 2011kl and ASASSN-15lh. *Astrophys. J. Letters* **817**, L8 (2016). `1601.01021`.

68. Kozyreva, A., Hirschi, R., Blinnikov, S. & den Hartogh, J. How much radioactive nickel does ASASSN-15lh require? *Mon. Not. R. Astron. Soc.* (2016). `1603.00335`.

69. Chatzopoulos, E. *et al.* Extreme Supernova Models for the Super-luminous Transient ASASSN-15lh. *Astrophys. J.* **828**, 94 (2016). `1603.06926`.

70. Metzger, B. D. & Stone, N. C. A bright year for tidal disruptions. *Mon. Not. R. Astron. Soc.* **461**, 948–966 (2016). `1506.03453`.

71. Coughlin, E. R. & Begelman, M. C. Hyperaccretion during Tidal Disruption Events: Weakly Bound Debris Envelopes and Jets. *Astrophys. J.* **781**, 82 (2014). `1312.5314`.

72. Roth, N., Kasen, D., Guillochon, J. & Ramirez-Ruiz, E. The X-Ray through Optical Fluxes and Line Strengths of Tidal Disruption Events. *Astrophys. J.* **827**, 3 (2016). `1510.08454`.

73. Hayasaki, K., Stone, N. & Loeb, A. Finite, intense accretion bursts from tidal disruption of stars on bound orbits. *Mon. Not. R. Astron. Soc.* **434**, 909–924 (2013). `1210.1333`.

74. Shiokawa, H., Krolik, J. H., Cheng, R. M., Piran, T. & Noble, S. C. General Relativistic Hydrodynamic Simulation of Accretion Flow from a Stellar Tidal Disruption. *Astrophys. J.* **804**, 85 (2015). `1501.04365`.

75. Hayasaki, K., Stone, N. C. & Loeb, A. Circularization of Tidally Disrupted Stars around Spinning Supermassive Black Holes. *ArXiv e-prints* (2015). `1501.05207`.

76. Guillochon, J. & Ramirez-Ruiz, E. A Dark Year for Tidal Disruption Events. *Astrophys. J.* **809**, 166 (2015). `1501.05306`.

77. Ulmer, A. Flares from the Tidal Disruption of Stars by Massive Black Holes. *Astrophys. J.* **514**, 180–187 (1999).

78. Strubbe, L. E. & Quataert, E. Optical flares from the tidal disruption of stars by massive black holes. *Mon. Not. R. Astron. Soc.* **400**, 2070–2084 (2009). `0905.3735`.

79. Kesden, M. Black-hole spin dependence in the light curves of tidal disruption events. *Phys.R. D* **86**, 064026 (2012). `1207.6401`.

80. Carter, B. & Luminet, J.-P. Tidal compression of a star by a large black hole. I Mechanical evolution and nuclear energy release by proton capture. *Astron. Astrophys.* **121**, 97–113 (1983).

81. Merritt, D., Alexander, T., Mikkola, S. & Will, C. M. Testing properties of the Galactic center black hole using stellar orbits. *Phys.R. D* **81**, 062002 (2010). `0911.4718`.

82. Beloborodov, A. M., Illarionov, A. F., Ivanov, P. B. & Polnarev, A. G. Angular momentum of a supermassive black hole in a dense star cluster. *Mon. Not. R. Astron. Soc.* **259**, 209–217 (1992).

83. Marck, J.-A. Solution to the Equations of Parallel Transport in Kerr Geometry; Tidal Tensor. *Proceedings of the Royal Society of London Series A* **385**, 431–438 (1983).

84. Yaron, O. & Gal-Yam, A. WISeREP - An Interactive Supernova Data Repository. *Publications of the Astronomical Society of the Pacific* **124**, 668–681 (2012). `1204.1891`.

85. Nicholl, M. *et al.* Slowly fading super-luminous supernovae that are not pair-instability explosions. *Nature* **502**, 346–349 (2013). `1310.4446`.

86. Holoien, T. W.-S. *et al.* ASASSN-15oi: A Rapidly Evolving, Luminous Tidal Disruption Event at 216 Mpc. *ArXiv e-prints* (2016). `1602.01088`.

87. Hatano, K., Branch, D., Fisher, A., Millard, J. & Baron, E. Ion Signatures in Supernova Spectra. *Astrophys. J. Supplements* **121**, 233–246 (1999). `astro-ph/9809236`.

88. Chornock, R. *et al.* The Ultraviolet-bright, Slowly Declining Transient PS1-11af as a Partial Tidal Disruption Event. *Astrophys. J.* **780**, 44 (2014). `1309.3009`.

89. Holoien, T. W.-S. *et al.* Six months of multiwavelength follow-up of the tidal disruption candidate ASASSN-14li and implied TDE rates from ASAS-SN. *Mon. Not. R. Astron. Soc.* **455**, 2918–2935 (2016). `1507.01598`.
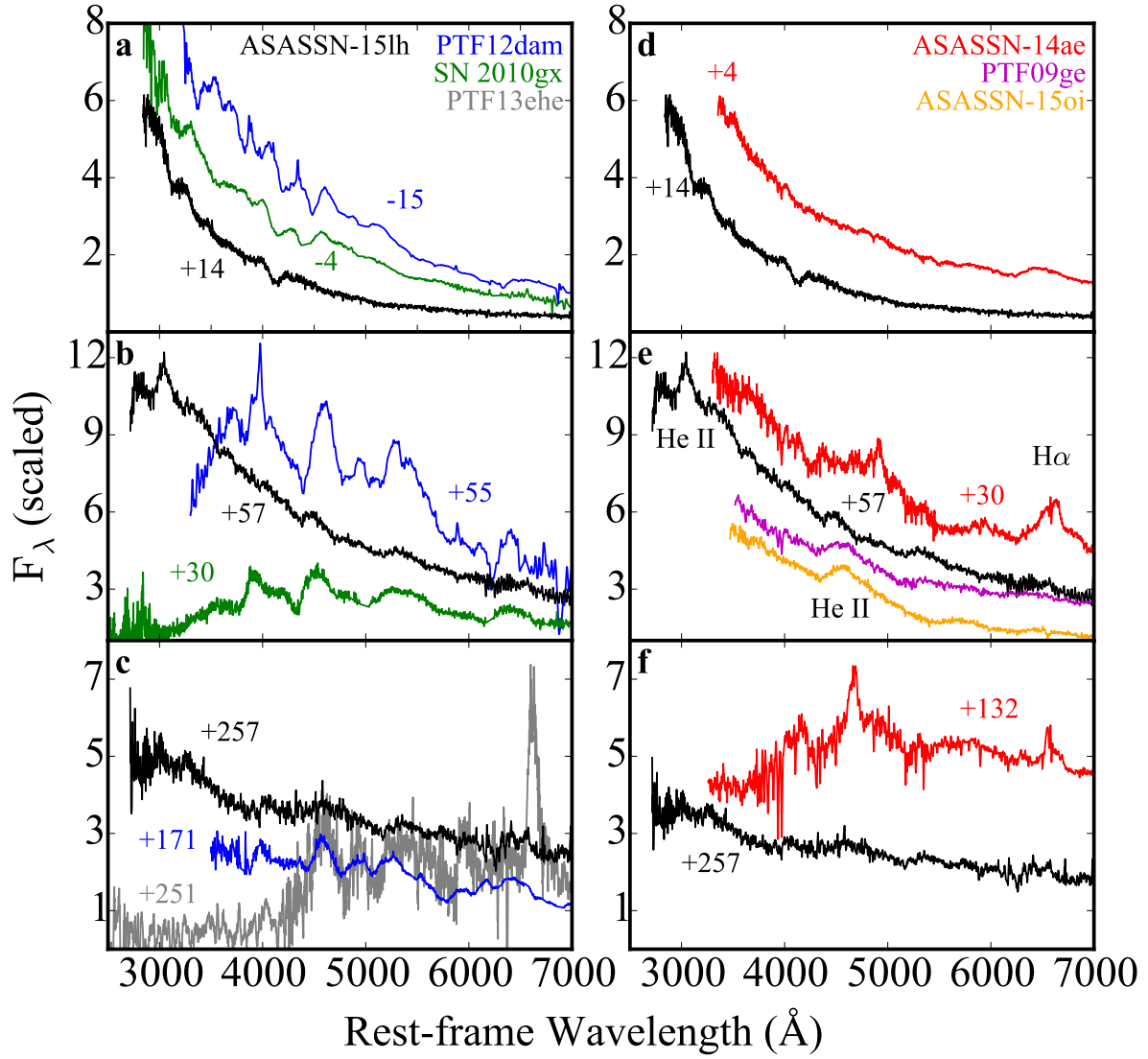
Supplementary Figure 1 | **Spectroscopic comparison of ASASSN-15lh with SLSNe and**

TDEs. The left panels compare spectra of ASASSN-15lh at different phases with those of SLSNe[17, 85, 28].

The right panels compare the same spectra with TDEs[5, 6, 86]. At early times (a), ASASSN-15lh

looks indeed similar to SLSNe[7] but lacks a strong O II feature. The later spectra (b,c) are very dif-

ferent from those of SLSNe and even at +257 days ASASSN-15lh is purely continuum-dominated

without any nebular features or signs of strong circumstellar interaction, such as in PTF13ehe[28].

Despite the differences with TDE spectra (d,e,f) there are also similarities, especially with TDEs

showing blueshifted He II (e), or even with the early spectrum of ASASSN-14ae (d). ASASSN-15lh

has H (Figure 1), but it is weaker than in ASASSN-14ae.
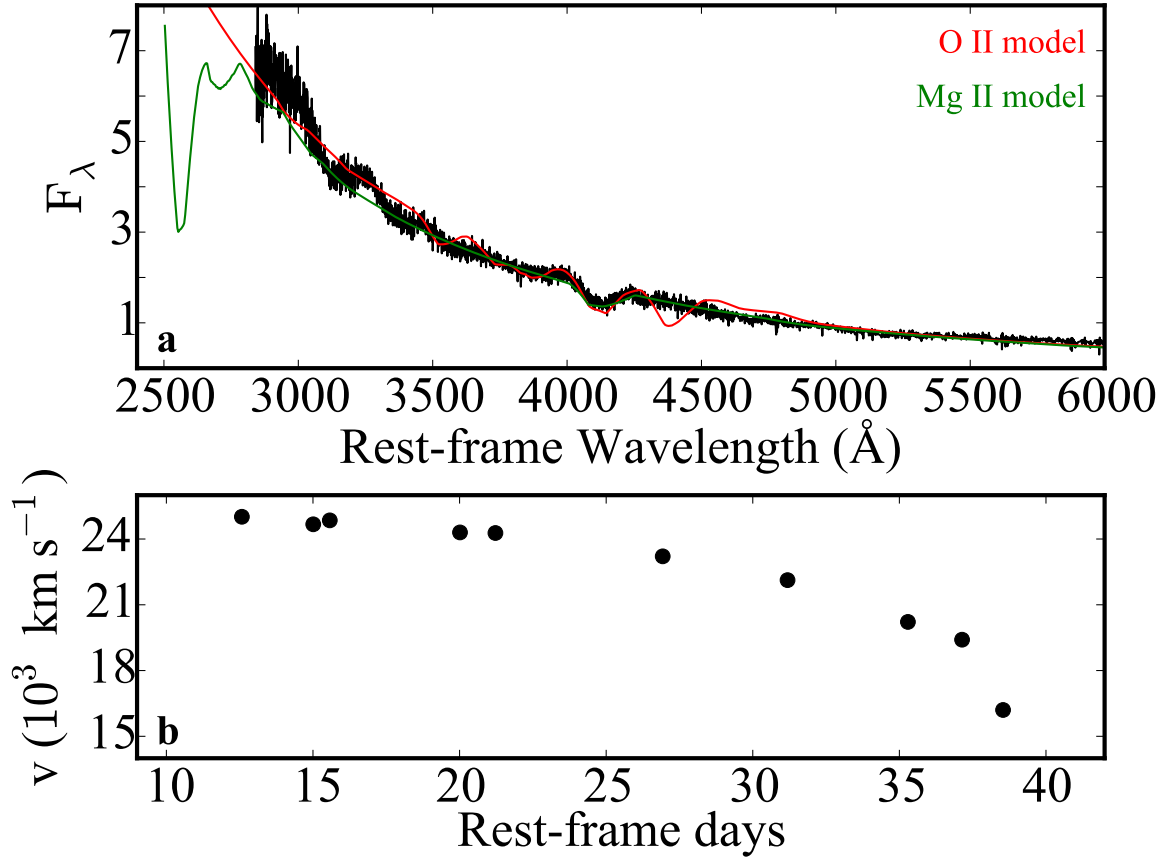
Supplementary Figure 2 | **The early phases of ASASSN-15lh.** (a) Modelling the spectra with SYNOW[87] and O II as in SLSNe[8, 15] is not possible as a strong feature at ~4400 Å is inevitable. A tentative identification of the strongest feature at ~4100 Å is Mg II, which however produces additional strong features in the UV. Such features (transient in nature) have been observed in a TDE candidate[88] and cannot be ruled out for the early phases of ASASSN-15lh, based on the available spectra. The use of SYNOW in this case is purely illustrative, as this code has not been made to model TDEs. (b) Velocity evolution of the absorption at ~4100 Å assuming it is Mg II. Another possibility for this feature is that it might be due to high-velocity He II[16]. In this case, the velocities are larger by ~12,000 km s^{-1}.
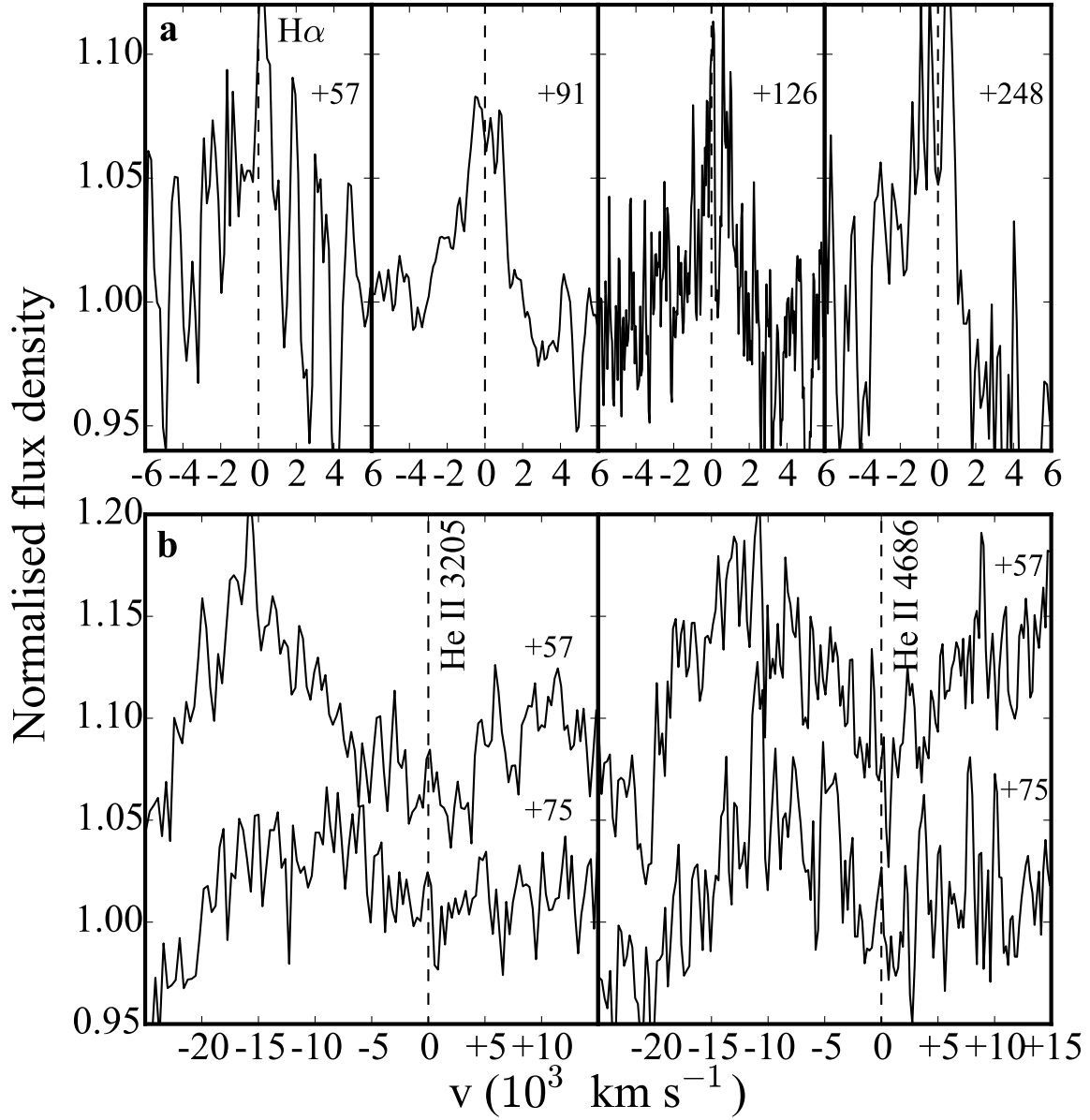
Supplementary Figure 3 | **Detection of H and possible detection of transient He in the spectra of ASASSN-15lh.** (a) Hα at representative epochs. The line is weak and the detection significance varies with signal-to-noise (see also Figure 1). However, there is no measurable

evolution in its strength (EW $\sim 4 - 8$ Å), and its presence cannot be excluded in any spectrum. (b)

The profiles of the lines identified as blueshifted He II at $+57$ and $+75$ days.
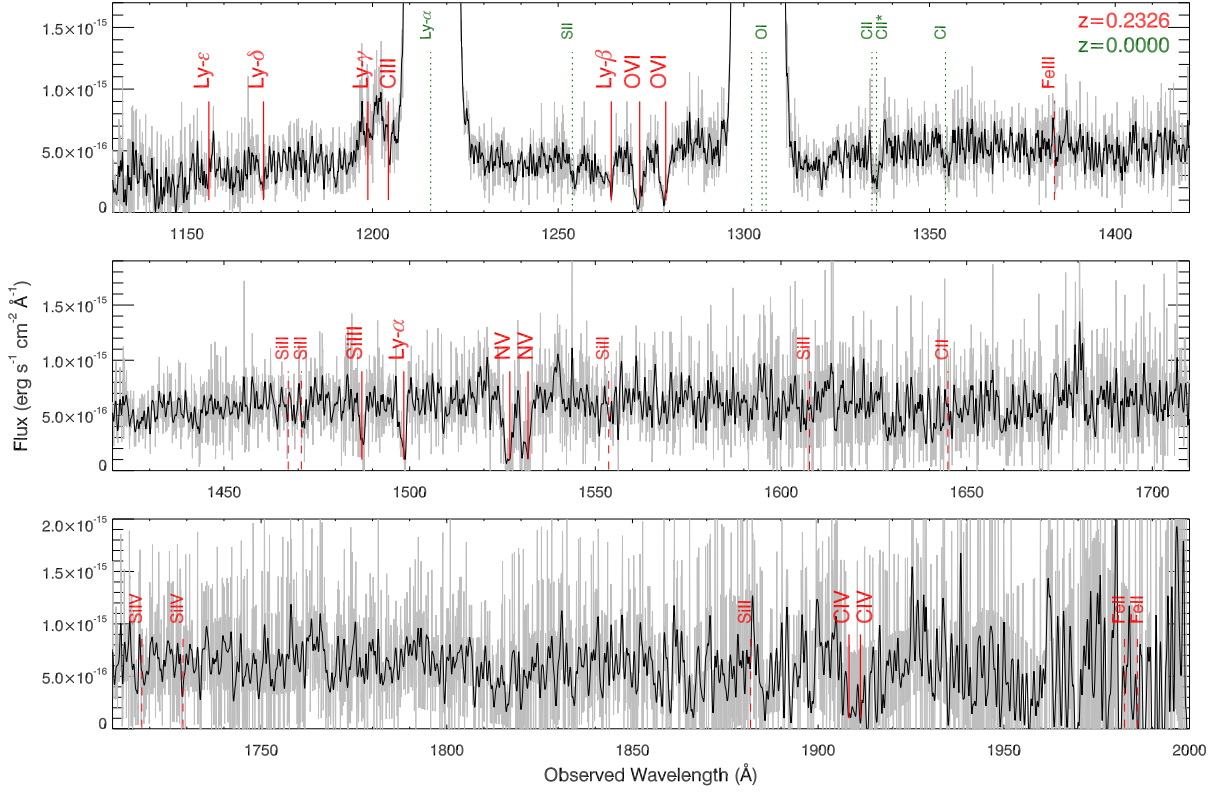
Supplementary Figure 4 | **An ultraviolet spectrum of ASASSN-15lh obtained with *HST*+COS at 168 rest-frame days past maximum.** We identify both local geocoronal lines (marked with green) and narrow absorption features associated with ASASSN-15lh at $z = 0.2326$ (red). Detections (marked with red solid lines), include Ly-α, Ly-β, Si III, C IV, and, notably, N V and O VI. The most prominent lines that are not detected are marked with a red dashed line.
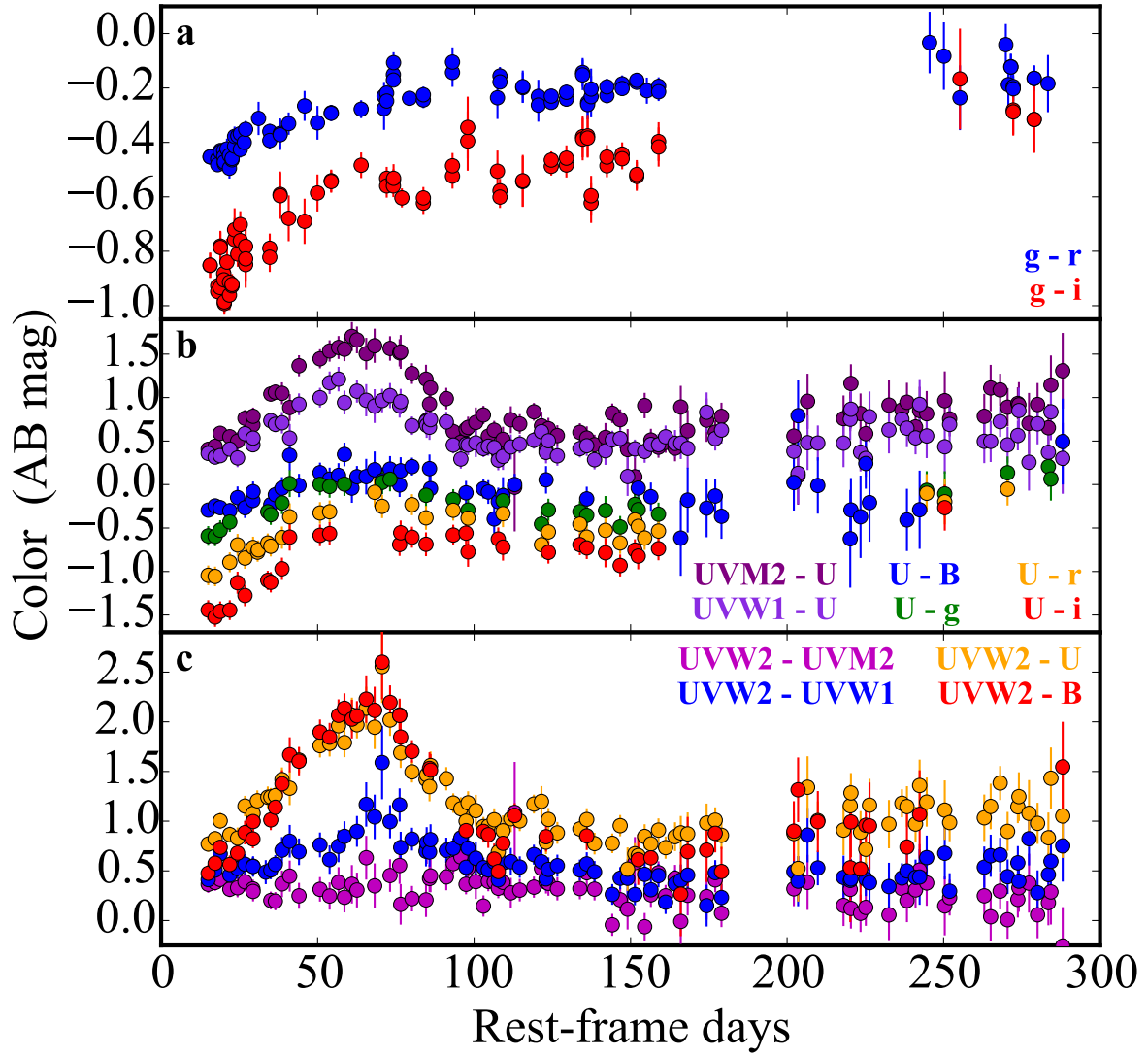
Supplementary Figure 5 | **The colour evolution of ASASSN-15lh.** We show optical colours with respect to g in panel (a), different UV and UV$-$optical colours with respect to U in panel (b), and UV colours with respect to $UVW2$ in panel (c). Errorbars represent 1σ uncertainties. Most

colours show a significant evolution to the red, peaking at 60 days past-maximum and corresponding to the UV minimum in Figure 2. Subsequently, the UV colours get bluer again. All colours remain fairly constant after day $+100$ and for a period of over 120 days.
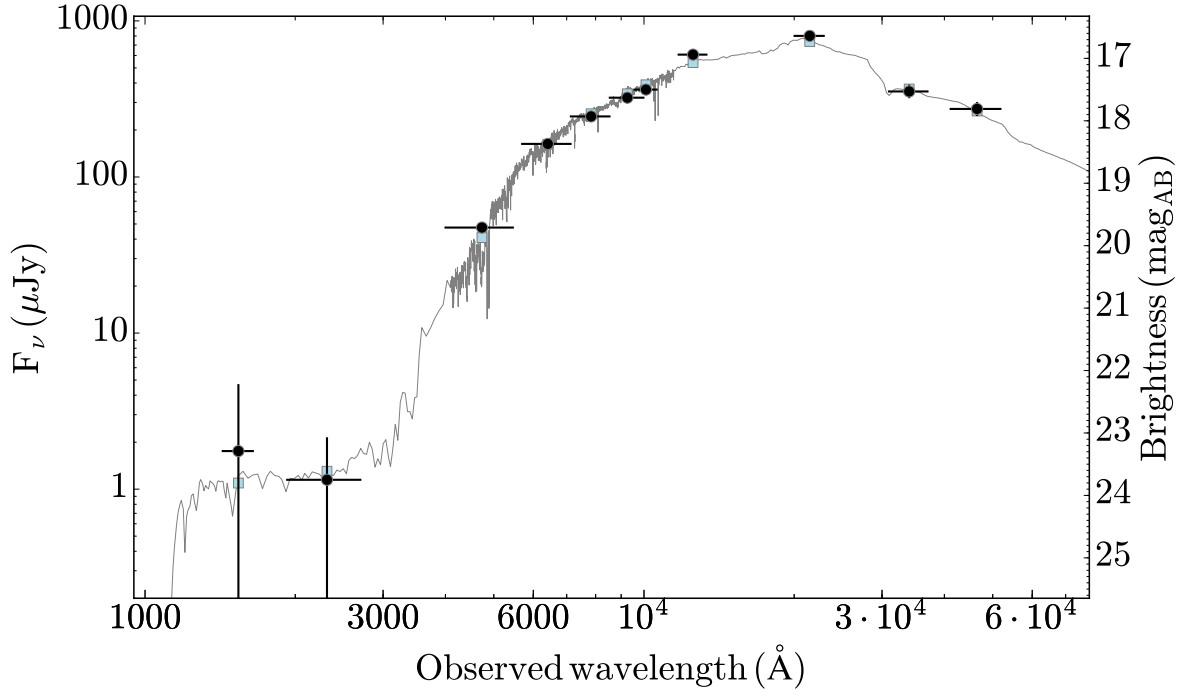
Supplementary Figure 6 | **SED fit for the host galaxy of ASASSN-15lh.** To perform the fit we are using the code *Le Phare* and photometric data all the way from the far-UV (GALEX) to the mid-IR (WISE). Shown is the best-fitting template (reduced $\chi^2 = 0.998$). The GALEX non-detections are shown here with the nominal SExtractor photometry errors.
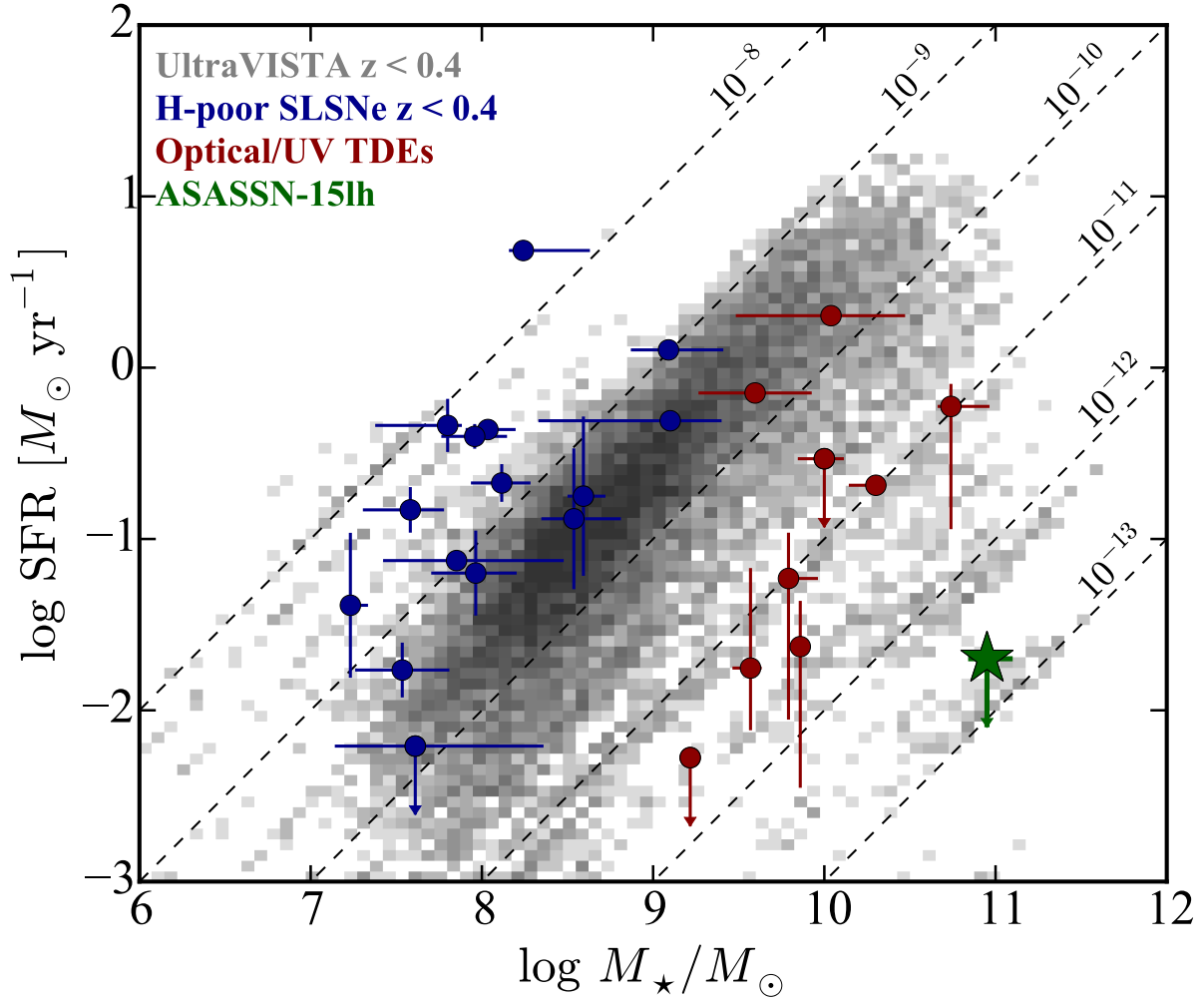
Supplementary Figure 7 | **The properties of the host galaxy of ASASSN-15lh compared to those of SLSNe[10, 11] and TDEs[5, 6, 89, 86].** For comparison, we show the general galaxy population at $z < 0.4$ from UltraVISTA and we have drawn lines of equal specific SFR. The location of ASASSN-15lh clearly stands out from those of SLSNe that are found in dwarf star-forming galaxies on or above the main sequence of star formation. The separation of ASASSN-15lh is 3 orders of magnitude in terms of specific SFR. At the same time, the host is significantly more massive from those of most optical TDEs, suggesting a large SMBH mass.
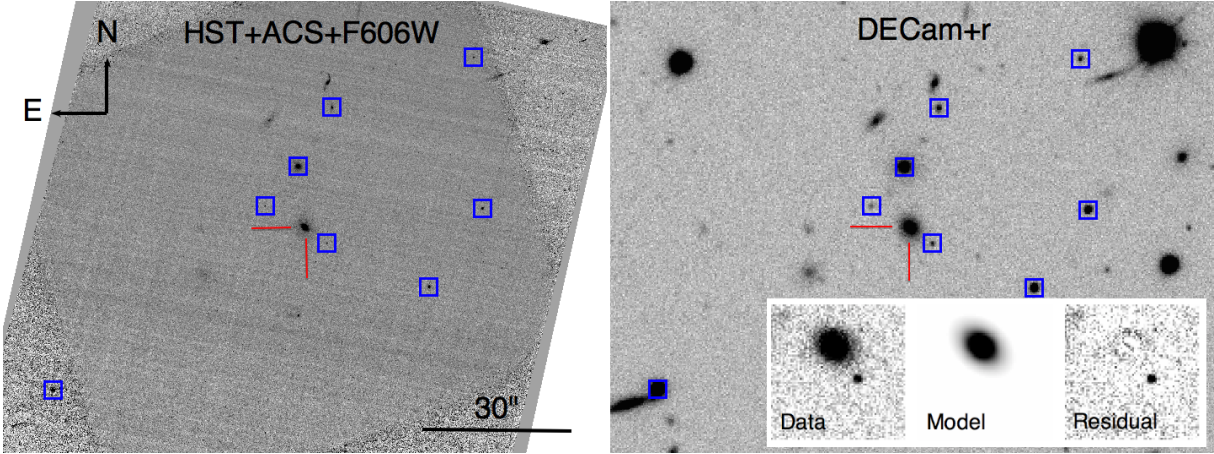
Supplementary Figure 8 | **The localisation of ASASSN-15lh in the nucleus of its host galaxy.** On the left is an *HST* image of ASASSN-15lh obtained at day +47. On the right is a DECam image from October 2014, several months before the transient appeared. The sources used to derive the geometric transformation between the frames are marked with blue squares. The inset shows a zoom in to the host together with a GALFIT model and the residual from the model fit. ASASSN-15lh has an offset of 36 ± 53 mas from the nucleus and it is thus consistent with the location of the central SMBH.

Line	λ_{obs} (Å)	offset (km/s) [a]	EW (Å)	EW$_{GRB}$ [b] (Å)	EW$_{SLSN}$ (Å)
O VI 1031	1271.57	-80 ± 12	1.97 ± 0.26	–	–
O VI 1037	1278.55	-80 ± 12	1.57 ± 0.24	–	–
S III 1206	1487.26	$+44 \pm 22$	0.79 ± 0.26	–	–
Ly-α	1498.26	0 ± 12	1.15 ± 0.32	73.0	–
N V 1238	1526.50	-117 ± 12	1.97 ± 0.41	0.14	–
N V 1242	1531.26	-117 ± 12	2.07 ± 0.43	0.07	–
Si II 1259	–	–	< 1.73	1.26	–
Si II 1304	–	–	< 2.21	2.29	–
C II 1334	–	–	< 2.56	1.73	–
Si IV 1393	–	–	< 2.75	0.95	–
Si II 1527	–	–	< 6.7	0.93	–
C IV/C IV 1548	–	-204 ± 92	3.08 ± 2.35	2.18	–
Fe II 1608	–	–	< 24.0	0.85	–
Fe II 2382	–	–	< 1.31	1.65	0.35 ± 0.03 [c]
Fe II 2600	–	–	< 3.65	1.85	0.29 ± 0.03 [c]
Mg II 2796	3445.67	$+8 \pm 8$	0.50 ± 0.05	1.71	2.6 ± 1.2 [d]
Mg II 2803	3454.46	$+14 \pm 10$	0.38 ± 0.05	1.47	– [d]

Supplementary Table 1 | **Absorption lines in the spectrum of ASASSN-15lh**. Upper limits are 3σ. EWs are in rest-frame. Notes: [a] The reference velocity was set to Ly-alpha ($z = 0.23253$).

[b] Based on a high S/N composite GRB afterglow spectrum[47]. Typical error for weak lines is 0.02 Å.

[c] Based only on PTF13ajg[46]. [d] Total value for the doublet, based on a sample of 13 events[46].

Date (UT)	Phase	Telescope+Instrument	Grism	Range (nm)
2015-06-22.7	+14.0	FTS+FLOYDS		325 - 930
2015-06-24.7	+15.6	ANU 2.3m+WiFeS	B3000+R3000	350 - 956
2015-07-01.6	+21.2	ANU 2.3m+WiFeS	B3000+R3000	350 - 956
2015-07-08.7	+26.9	ANU 2.3m+WiFeS	B3000+R3000	350 - 956
2015-07-21.3	+37.1	VLT+FORS2	300V	445 - 865
2015-07-31.5	+45.4	ANU 2.3m+WiFeS	B3000+R3000	350 - 956
2015-08-14.3	+56.6	NTT+EFOSC2	GR#11+16	334 - 999
2015-09-06.0	+75.0	NTT+EFOSC2	GR#11+16	334 - 999
2015-09-16.1	+83.2	NTT+EFOSC2 [a]	GR#11+16	334 - 999
2015-09-23.2	+89.0	NTT+EFOSC2	GR#11+16	334 - 999
2015-09-25.1	+90.6	VLT+FORS2	300V	445 - 865
2015-10-11.1	+103.6	NTT+EFOSC2 [b]	GR#11	334 - 745
2015-10-13.2	+105.2	NTT+EFOSC2 [b]	GR#16	599 - 999
2015-11-08.0	+126.2	Magellan+IMACS	Gri-300-17.5	400-999
2015-11-18.1	+134.3	NTT+EFOSC2	GR#13	365 - 924
2015-12-16.0	+157.0	NTT+EFOSC2	GR#11+16	334 - 999
2016-04-06.3	+248.1	NTT+EFOSC2	GR#11+16	334 - 999
2016-04-15.3	+256.2	NTT+EFOSC2	GR#11+16	334 - 999

Supplementary Table 2 | **Log of spectra**. Notes: [a] Low S/N; not used. [b] Combined to a single spectrum.